OXFORD

Journal of Petrology, 2025, **66**, egaf029
https://doi.org/10.1093/petrology/egaf029
ADVANCE ACCESS PUBLICATION DATE 27 MARCH 2025
Original Manuscript

A General Conceptual Petrological Model for the Subsolidus Transformation of Chromitite with Application and Implications

ANTONIO GARCIA-CASCO [1,*], NÚRIA PUJOL-SOLÀ[1], IRENE NOVO-FERNÁNDEZ[1], RICARDO ARENAS[2], ESTHER ROJO-PÉREZ[3], AITOR CAMBESES[1], JOSÉ FRANCISCO MOLINA[1], SONIA SÁNCHEZ MARTÍNEZ[2], DIEGO DOMÍNGUEZ-CARRETERO[4], GABRIEL IGLESIAS[2] and JOAQUÍN A. PROENZA[4]

[1]Department of Mineralogy and Petrology, University of Granada, Av. Fuentenueva sn, 18071 Granada, Spain
[2]Department of Mineralogy and Petrology, Complutense University, C. de José Antonio Novais, 12, Moncloa - Aravaca, 28040 Madrid, Spain
[3]Senckenberg Naturhistorische Sammlungen Dresden, Königsbrücker Landstraße 159, 01109 Dresden, Germany
[4]Departament de Mineralogia, Petrologia i Geologia Aplicada, Facultat de Ciències de la Terra, Universitat de Barcelona, Martí i Franquès, s/n, Distrito de Les Corts, 08028 Barcelona, Spain

*Corresponding author. Telephone: +34 958 246613. E-mail: agcasco@ugr.es

A general petrologic model for the transformation of chromitite in the FeO–MgO–Al_2O_3–Cr_2O_3–SiO_2–H_2O (FMACrSH) system is presented based in mass-balance and thermodynamic constraints. In the model, the transformation of chromitite reaches the common Cr-spinel+chlorite assemblage of transformed chromitites upon reaction with external fluid. This metasomatic process takes place in two major sequential steps involving a net-transfer reaction of olivine consumption first ensued by Cr-spinel+chlorite dissolution–precipitation. The first step is completed early in the hydration/metasomatic process producing new Cr-spinel (+chlorite±brucite) with restricted composition close to the composition of reacting mantle Cr-spinel as a function of Cr-spinel/olivine ratio and the stoichiometric coefficients of olivine and Cr-spinel in the net-transfer reaction. The second transformation step, triggered upon exhaustion of olivine, is protracted and continuously produces increasing chlorite and decreasing Cr-spinel contents, the latter with continued more deviated composition from reacting mantle Cr-spinel, as a function of continued infiltration of external fluid. The mass-balance model does not prejudice transformation under isothermal-isobaric conditions, heating, or cooling, but thermodynamic calculations confirm that all these thermal scenarios are possible for the generation of the predicted mineral assemblages and compositions. These calculations demonstrate that extreme Cr-spinel compositions are a strong function of decreasing spinel volume upon reaction progress at reaction sites under strongly overstepped conditions. The application of the model to mantle chromitites of the Cadomian Calzadilla metaophiolite (Ossa-Morena Complex, SW Iberia) allows reinterpreting the thermal scenario for chromitite transformation in a context of prograde metamorphism at near-isothermal-isobaric conditions. Proposals of cooling during transformation of regionally metamorphosed chromitites should be revisited in light of the petrologic model offered.

Key words: Alteration; chromitite; metamorphism; ophiolite; transformation

INTRODUCTION

Unlike silicate-dominated ultramafic rocks of the lithospheric mantle, metamorphism of associated mantle chromitite orebodies is not so commonly addressed in the literature (Suita & Strieder, 1996; Proenza *et al.*, 2004, 2008; Arai *et al.*, 2006; González-Jiménez *et al.*, 2009, 2017a; Merlini *et al.*, 2009; Gervilla *et al.*, 2012, 2019; Barra *et al.*, 2014; Colás *et al.*, 2016, 2017, 2019, 2020; Pujol-Solà *et al.*, 2021; Eslami *et al.*, 2023). Mantle chromitite orebodies are typical of the oceanic mantle sections of ophiolitic units accreted to arcs or the continental crust, but they are also present in the subcontinental lithospheric mantle (Fig. 1). They form at high temperature (>1200°C; green dot in Fig. 1) during the magmatic structuration of oceanic lithosphere, most commonly in forearcs (Leblanc & Nicolas, 1992; González-Jiménez *et al.*, 2014; Arai & Miura, 2016 and references therein) but potentially also in the abyssal (e.g. Arai & Matsukage, 1998) and backarc settings (e.g. González-Jiménez *et al.*, 2015a, 2015b; Hernández-González *et al.*, 2020; Mendi *et al.*, 2020; Ramírez-Cárdenas *et al.*, 2024) and during magmatic processes triggered in the sub-continental lithospheric mantle (SCLM; Torres-Ruiz *et al.*, 1996; González-Jiménez *et al.*, 2017b; Malitch *et al.*, 2017). Their mineral assemblages are dominated by chromium-spinel (Cr-Spl) solid solution ($(Mg,Fe)(Al,Cr)_2O_4$, hereinafter abbreviated spinel or Spl) with moderate to high molar MgO/(MgO + FeO) (= Mg) and $Cr_2O_3/(Cr_2O_3 + Al_2O_3)$ (= Cr#), both typically in the range from 0.4 to 0.8 (e.g. González-Jiménez *et al.*, 2014; Zhou *et al.*, 2014; Zhang *et al.*, 2024), plus lower amounts of sulphides, metals and alloys. Variable amount of olivine ($(Mg,Fe)_2SiO_4$) with molar Mg# of around 0.9 is characteristically present, being the spinel-olivine assemblage the most typical of chromitite (Leblanc & Nicolas, 1992; González-Jiménez *et al.*, 2014; Arai & Miura, 2016 and references therein). Once formed during magmatic accretion

RECEIVED OCTOBER 20, 2024; **REVISED** JANUARY 24, 2025; **ACCEPTED** MARCH 23, 2025

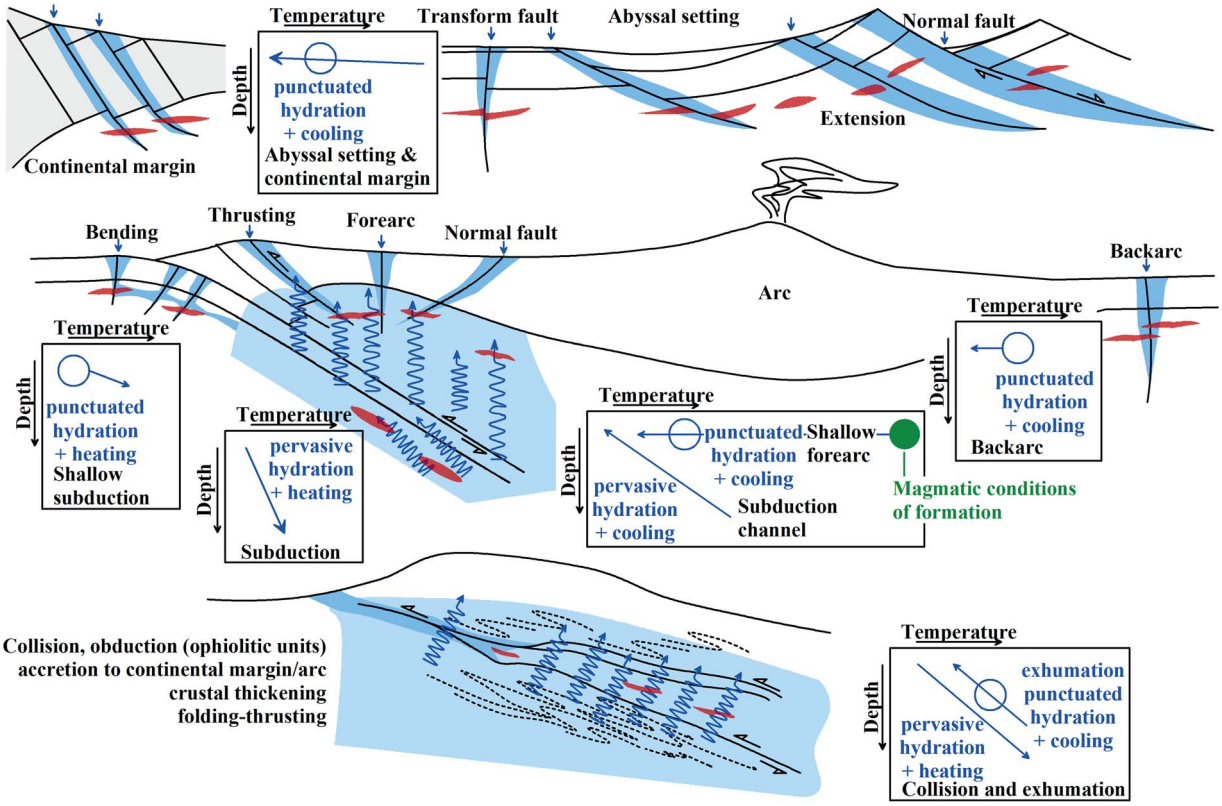

Fig. 1. Sketches illustrating the varied tectonic-metamorphic scenarios for the transformation of mantle chromitites (red pods) upon fluid infiltration (blue arrows) and hydration (bluish regions). Note fluid infiltration from above (non-orogenic contexts) and from below (orogenic contexts). A green circle in the temperature-depth diagram for the fore-arc (which is the main locus of formation of mantle chromitites; see text) represents generalized magmatic conditions of formation. Similar conditions should be considered in all other T-depth diagrams for oceanic chromitites (greater depth for the SCLM environment). See text for explanation.

under a high geothermal gradient, the oceanic lithosphere cools down until a stable mature oceanic geotherm is eventually achieved. During this process, chromitite may undergo hydration, triggering metamorphic transformation of the spinel+olivine assemblage (Figs 1 and 2). Almost universally, such hydration upon cooling generates a mineral assemblage strongly dominated by new spinel with Cr- and Fe-richer composition and chlorite (Suita & Strieder, 1996; Proenza *et al.*, 1999, 2004; Arai *et al.*, 2006; González-Jiménez *et al.*, 2009; Merlini *et al.*, 2009; Gervilla *et al.*, 2012, 2019; Merinero *et al.*, 2014; Colás *et al.*, 2016, 2017, 2019; Pujol-Solà *et al.*, 2021). Similar processes attend chromitite transformation during cooling of the SCLM, either at mantle depths in stretched continental lithosphere or upon tectonic accretion during orogenic processes (González-Jiménez *et al.*, 2014; Malitch *et al.*, 2017 and references therein).

It should be noted that the reaction processes involving mantle spinel and olivine in chromitite are strongly overstepped and intrinsically retrograde relative to the conditions of magmatic formation at >1000°C, either if the transformation process takes place at isothermal-isobaric conditions or during increasing or decreasing temperature in the tectonic-metamorphic contexts depicted in Fig. 1. Hence, the mineral-textural product of this type of process would look like a retrograde feature whatever the thermal history undergone during transformation. This obvious statement has not been fully appreciated in case studies of regionally metamorphosed chromitites that have suffered tectonic burial, as in subduction zones and collisional settings (Suita & Strieder, 1996; Proenza *et al.*, 2004, 2008; Gervilla *et al.*, 2012; Colás *et al.*, 2017, 2019, 2020; and references therein). In general, chromitite transformation in these cases has been considered to develop after attainment of peak metamorphic conditions, i.e. during cooling and exhumation from depth. This conclusion implies that the necessary infiltration of fluid occurred during retrogression only (e.g. Gervilla *et al.*, 2012; Colás *et al.*, 2017, 2019; and references therein). The main basis for these proposals is the textural-mineral development, characterized by progressive replacements of mantle spinel by chlorite and increasingly higher Fe and Cr contents in spinel, under the premise that these compositions form at lower temperature than Mg-Al-richer spinel (Proenza *et al.*, 2004; González-Jiménez *et al.*, 2009; Merlini *et al.*, 2009; Pujol-Solà *et al.*, 2021; Eslami *et al.*, 2023). In spite of some evidence for open system conditions during transformation (e.g. Colás *et al.*, 2017), such premise stems from thermodynamic calculations for fixed bulk composition (i.e. isochemical P–T phase diagrams, also known as P–T pseudosections) and the fact that similar textural-mineral development is observed in chromitite transformed in cooled shallow abyssal/forearc/backarc environments (e.g. Gervilla *et al.*, 2012; Colás *et al.*, 2019). Thus, the comparable changes in composition of spinel during progressive transformation in the contrasted thermal–tectonic scenarios of Fig. 1, framed in terms of textural position and evolution (e.g. external rims, rims, mantles, cores of grains), seems to have helped to strengthen the generalized view that decreasing temperature is the main control on reaction progress. This view is challenged here after consideration of the effects of isothermal-isobaric conditions, cooling and heating in closed and open systems.

Varied geodynamic scenarios where hydration of mantle chromitite is possible along retrograde or prograde P–T paths,

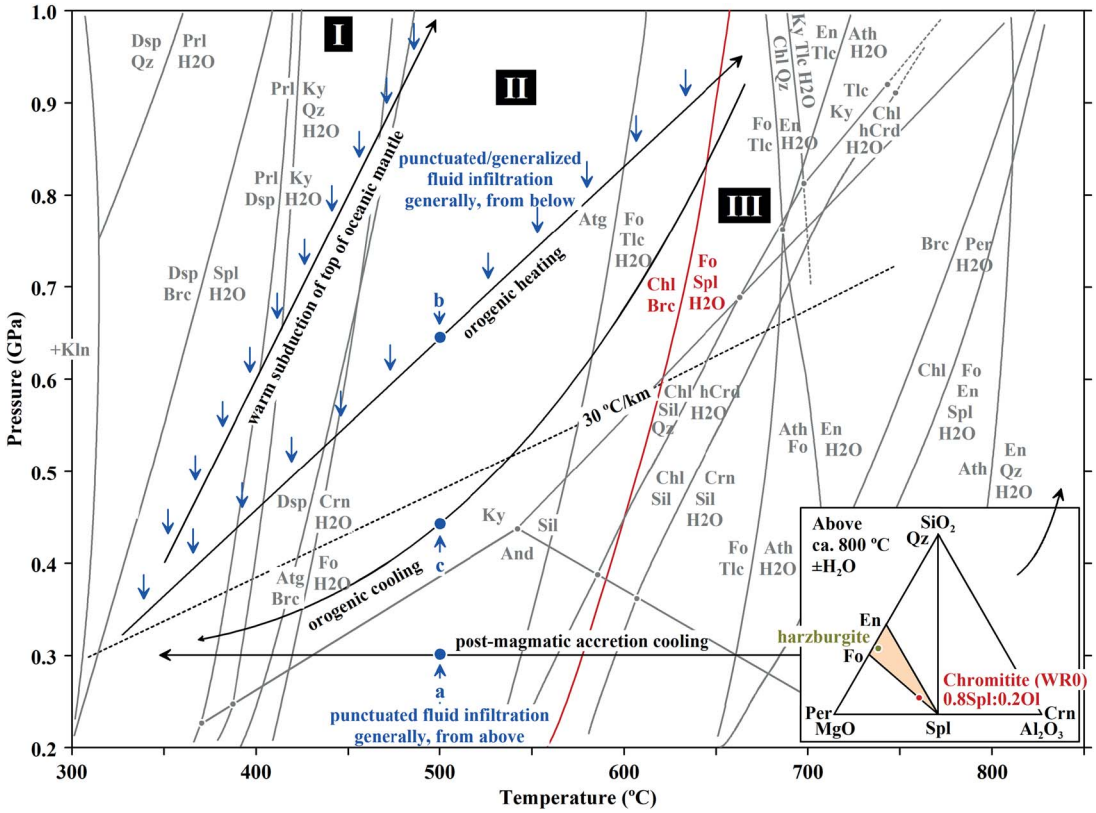

Fig. 2. P–T grid with reactions relevant for model chromitite (red, eq. 1) and other rocks (grey) in the MASH system. Phase relations with cummingtonite, gedrite, staurolite, sapphirine and anhydrous cordierite, which pertain to the high-SiO_2, high-Al_2O_3 field of the composition space at >ca. 700°C, have been omitted for clarity. The terminal reaction of chlorite is from Jenkins (1981). The triangular phase diagram (inset) is for P–T conditions above the maximum stabilities of chlorite and anthophyllite. A model mixture of spinel and olivine with 0.8 and 0.2 mole fractions, respectively, is represented in this diagram (red dot). General phase diagrams for fields I and II (below) and III (above; eq. 1) are presented in Fig. 3. The metamorphic effects of isobaric cooling of oceanic lithosphere after magmatic accretion (point a) and orogenic heating (b) and cooling (c) upon punctuated or pervasive fluid infiltration are discussed in the text.

or at isothermal-isobaric conditions, are depicted in Fig. 1. In general, hydration is eventual, episodic and punctuated along normal and transform faults that focalize seawater infiltration in the crust and shallow mantle of extended continental lithosphere and the abyssal and back-arc settings of the oceanic lithosphere (Fig. 1; e.g. Nishi, 2015; Liu *et al.*, 2017; Prigent *et al.*, 2020; Zhu *et al.*, 2021). For a given episode of punctuated fluid infiltration, temperature and pressure are expected to be near constant. The shallow mantle of forearc lithosphere is also affected by similar punctuated hydration, but deep-seated fluids emanating from the subduction slab may cause generalized rather than punctuated hydration down to great depth in the forearc mantle (Fig. 1; Epstein *et al.*, 2024). At trenches, the oceanic lithosphere fractures upon bending, causing punctuated hydration at expected near-constant temperature, or more pervasive hydration during heating upon initial shallow subduction of these parts of the lithosphere (Fig. 1; Miller *et al.*, 2021; Mark *et al.*, 2023). Continued subduction to greater depths is characterized by energic fluid flow triggered by dehydration at greater depth along the slab, promoting generalized (near-) full hydration of the subducting metaultramafic rocks (i.e. serpentinites) and metabasites (blueschist, eclogite; Fig. 1; Sorensen & Grossman, 1989; Penniston-Dorland *et al.*, 2012a, 2012b, 2014; Hyppolito *et al.*, 2016; Angiboust *et al.*, 2017, 2021; Manning & Frezzotti, 2020; Epstein *et al.*, 2021; Muñoz-Montecinos *et al.*, 2020, 2021). Similarly, continental/block convergence triggers collision-related regional tectono-metamorphism and generalized fluid flow due to dehydration of the involved metamorphic units comprising the orogenic wedge, allowing hydration of ophiolitic units (Fig. 1; Shervais, 2001; Shervais *et al.*, 2011; Wakabayashi, 2011, 2019; Festa *et al.*, 2012). As in the subduction environment, generalized fluid flow and (near-) full hydration during prograde metamorphism of ophiolitic units involved in collisional settings is demonstrated by near-full hydration of associated prograde greenschist, amphibolite and serpentinite (e.g. Novo-Fernández *et al.*, 2024). Further fluid flow during exhumation in the subduction and collision settings affects the metamorphosed ophiolitic fragments/blocks/units accreted to the subduction channel/upper plate (Fig. 1). However, it is generally punctuated and limited, judging from the generally local partial retrograde overprints of associated metabasites (Fig. 1; e.g. García-Casco *et al.*, 2002, 2006; Garcia-Casco *et al.*, 2008; Blanco-Quintero *et al.*, 2011).

In this paper, we offer a conceptual petrological analysis of chromitite transformation that is general and applicable to the (near-)isobaric-isothermal, heating and cooling conditions expected at the different geodynamic scenarios depicted in Fig. 1. The model, constructed to evaluate the consequences of a chemically changing medium initially characterized by a mixture of mantle spinel and olivine, is based on a mass-balance approach in the FeO–MgO–Al_2O_3–Cr_2O_3–SiO_2–H_2O (FMACrSH) system. First and foremost, the model considers the effects of reaction stoichiometry on exhaustion of olivine in a spinel-dominated system and the nature of the ensuing

olivine-lacking reaction process. The progressive changes in the composition of local reaction sites upon reaction progress and on spinel composition are evaluated by means of a mass-balance analysis of reaction progress during and after olivine consumption. The thermodynamic validation of the model is addressed, despite problems with the thermodynamic properties of Cr-bearing chlorite solid solution. In the second part of this contribution, the predictions of the model are compared to the product of transformation in a natural case study of mantle chromitite in a collisional setting. The Neoproterozoic Calzadilla Ophiolite of southwestern Iberia formed in an oceanic forearc setting and underwent subsequent tectonic burial and heating during the Cadomian orogenic cycle (Arenas *et al.*, 2018, 2024; Novo-Fernández *et al.*, 2024 and references therein). However, the chromitite bodies of the mantle section of the ophiolite suffered transformations that have been related to sequential hydration+cooling after the metamorphic peak (Merinero *et al.*, 2014). We revisit this case study by means of detailed chemical-textural data framed in the predictions of the general petrologic model.

METHODS

Back-scattered electron (BSE) images, quantitative electronprobe microanalyses and X-ray (XR) elemental maps were obtained with a JEOL JXA-8230 at the Centres Científics i Tecnològics, Barcelona University (CCiTUB), operated in wavelength-dispersive spectroscopy (WDS) mode. Operating conditions for point analyses were 20 kV acceleration potential, 15 nA beam current, focused beam and 20 seconds/element (see Pujol-Solà *et al.*, 2021 for further details). Spinel analyses were normalized to 4 oxygens and 3 cations, while the analyses of chlorite were normalized to 20 oxygens, 16(OH) and 20 cations (Supplementary Table S1 and EarthChem Library link). Fe^{3+} content was estimated by stoichiometry. Atoms per formula unit is abbreviated apfu. X-ray maps were collected using the EPMA operated in WDS mode by stage scanning, with an accelerating voltage of 20 kV, beam current of 300 nA, dwell time of 20 ms per pixel, and pixel sizes (point spacing) of 0.38 to 2.5 μm. Experiments have demonstrated that short counting time (milliseconds rather than seconds) precludes beam damage at high beam current (García–Casco, 2007). The raw counts were transformed into oxide wt % with the ZAF correction. All maps were converted into molar oxide and atomic proportions and manipulated with DWImager software (see García-Casco, 2007; Torres-Roldán & Garcia-Casco, N.D.). This software was used to extract the bulk-compositions of the scanned areas and micro-domains. Reactions and tetrahedral and triangular projections have been obtained using algebraic methods (matrix analysis; e.g. Spear *et al.*, 1982) with CSpace (Torres-Roldan *et al.*, 2000; see also Garcia-Casco *et al.*, 2020) and Excel softwares. In the end-member system $MgO–Al_2O_3–SiO_2–H_2O$ (MASH) (system components = 4), stoichiometric coefficients of reactions among 5 selected phases (e.g. forsterite, spinel, chlorite, brucite and H_2O fluid, eq. 6 below) are straightforwardly found by matrix analysis. Bulk rock compositions in the 6-component system $FeO–MgO–Al_2O_3–Cr_2O_3–SiO_2–H_2O$ (FMACrSH) were algebraically mapped in new 6-dimensional coordinate systems defined by Mg–Al-bearing mineral end-members, exchange vectors $Cr_2O_3(Al_2O_3)_{-1}$ and $FeO(MgO)_{-1}$ (hereafter abbreviated $FeMg_{-1}$ and $CrAl_{-1}$, respectively) and H2O fluid, such as in eq. 11. Whole-rock compositions developed upon metasomatic MgO-loss from, or SiO_2-addition in, model chromitite (0.8:0.2 spinel/olivine ratio, molar units, WR0 below) were calculated in the FMACrSH system iteratively until an assemblage made of spinel and chlorite is reached (e.g. eq. 18 below). Most calculations were performed in molar units, but some are offered in oxy-equivalent units (e.g. eq. 19 below) to approximate the volume proportions of the solid phases (Brady & Stout, 1980; Thompson, 1982; Garcia-Casco *et al.*, 2020). These calculations were combined with calculations involving Fe–Mg and Al–Cr exchanges between olivine and spinel and chlorite and spinel using varied distribution coefficients (K_{Ds}), as justified below. Triangular and tetrahedral phase diagrams for the 6-component FMACrSH system involve projection from phases and exchange vectors, as indicated in the corresponding figures. Thermodynamic calculations have been performed using GeoPS v3.5.4 (Xiang & Connolly, 2022) and the thermodynamic dataset HP633 (Holland & Powell, 2011) and associated solutions models for olivine, orthopyroxene, spinel and garnet (Holland *et al.*, 2018), plus chlorite, chloritoid, staurolite, cordierite (White *et al.*, 2014) and talc (ideal Fe–Mg solution) and H_2O-fluid (Holland & Powell, 1998). Mineral abbreviations are after Warr (2021).

GENERAL PETROLOGIC MODEL

Our approach is to develop a model and, as such, it is an approximation that cannot perfectly describe the natural world. The lack of thermodynamic solution models for Cr-chlorite is a handicap for calculating phase relations that approximate geologic systems. The lack of consideration of other potentially important components, notably Ca and Ti, does not allow the involvement of minerals like clinopyroxene, Ca-clinoamphibole, rutile and ilmenite. However, these minerals are generally scarce, and in many cases only locally present as inclusions within Cr-spinel (Melcher *et al.*, 1997; Borisova *et al.*, 2012; Zhou *et al.*, 2014; Rollinson *et al.*, 2018; Liu *et al.*, 2019). Even if these minerals would trigger reactions not considered in this paper, the basic relations for the model Ca-Ti-absent case are retained due to their scarcity compared to olivine, spinel and chlorite, making the calculated relations in the Ca-Ti-lacking system applicable for a general case. The fluid has been treated as pure H_2O due to the general lack (or extreme scarcity) of carbonates and graphite/diamond in transformed chromitites. The speciation of H_2O-fluid and its effect on metasomatic transformation of chromitite has only been addressed qualitatively. Variation in fluid composition would drive an increase in the thermodynamic variance of all fluid-bearing assemblages, but the calculated trends in mineral associations and mineral composition (reaction progress) would not change. Oxidation may take place due to the eventual high fO_2 of infiltrating fluid, leading to the formation of Cr-Fe^{3+} spinel (ferrian chromite, Cr-magnetite and magnetite). However, in most transformed chromitites the process of oxidation is late and generally unrelated to previous reaction steps characterized by low fO_2 fluid (Gervilla *et al.*, 2012 and references therein). In what follows we concentrate on a model $Ca–Ti–C–CO_2–CH_4–Fe_2O_3$-free system FMACrSH.

Equilibrium is assumed all through the following theoretical development. For closed systems, this implies that the effective bulk composition of the phase assemblages is fixed. For open systems, phase assemblage transformation is triggered by shifts in the effective bulk composition. Hence, we do not consider the possibility that the system is divided in subsystems. For example, we do not consider an olivine-rich subsystem in a spinel-olivine mixture dominated by spinel (chromitite). In such a case, the transformation of olivine may produce serpentine-rich assemblages that, as demonstrated below, are not predicted in a model chromitite.

Closed system except for H_2O

The petrological consequences of total hydration of chromitite at moderate to low temperature are explored in Fig. 2, where reactions in the simple $MgO–Al_2O_3–SiO_2–H_2O$ (MASH) system are shown. These phase relations are applicable to chromitite with additional FeO and Cr_2O_3 components and will not change significantly because these two components are preferentially fractionated only in one phase (spinel). However, there may be complications at higher temperature derived from the potential stability of Fe–Mg amphiboles, staurolite, cordierite and sapphirine, among other phases. But, for temperatures lower than about 700°C to 750°C, the consideration of FeO and Cr_2O_3 would simply lead to an increase in the thermodynamic variance of the assemblages shown. Fig. 2 also shows a triangular phase diagram that corresponds to P–T conditions above the maximum stabilities of chlorite and anthophyllite, i.e. above ca. 800°C. In this ternary diagram, primary chromitite corresponds, essentially, to mixtures of spinel and olivine that plot along the Spl–Ol tie-line of the Spl–Ol–Opx tie-triangle (i.e. mole Opx = 0), as opposed to associated harzburgitic rocks. Detailed inspection of the P–T grid of Fig. 2 shows that hydrated model chromitite will suffer only one reaction (red in Fig. 2) in the whole represented P–T window:

$$Ol + Spl + H_2O = Chl + Brc. \quad (1)$$

That eq. 1 is the only reaction affecting model chromitite, with all other reactions affecting other types of rock, implies a singular behaviour that has important petrological consequences upon hydration of chromitites. The main one is that the mineral assemblage of chromitite will only differ above and below this reaction, but not within the P–T fields above and below. In other words, anhydrous or hydrous phases, such us serpentine group minerals, talc, diaspore or corundum do not form in model chromitite, even if they do in varied assemblages below and above eq. 1 in associated rocks such as hydrated mantle peridotites and pyroxenites. This is illustrated in the three vertical series of phase diagrams illustrated in Fig. 3, where the phase relations are constructed in the FMACrSH system, provided that projections from the exchange vectors $FeMg_{-1}$ and $CrAl_{-1}$ to warrant mass-balance and stoichiometric requirements (see Fisher, 1993). This procedure makes collinear all end-members (compositional range) of spinel solid solution and, hence, all types of primary and non-primary spinel compositions considered here plot in a single point in the MgO'-Al_2O_3'-SiO_2' projection. Furthermore, projection from exchange vectors may lead to cross-cutting tie-lines, implying the potential coexistence of more than three phases for a given bulk-rock composition, a scenario that has been omitted in Fig. 3 for clarity.

The three vertical panels in Fig. 3 correspond, respectively, to fields I, II and III of the P–T diagram of Fig. 2. Fields I and II (separated by eq. 4) are located on the low-T side of eq. 1 in Fig. 2, while field III is above this reaction. Note that field II corresponds to hydration at 500°C during punctuated or generalized fluid infiltration along (a) an isobaric cooling P–T path characteristic of the oceanic lithosphere after magmatic accretion, (b) an orogenic prograde P–T path and (c) an orogenic post-peak retrograde path (points a, b and c, respectively, in Fig. 2). Given the lack of other intervening reactions, all three P–T and tectonic scenarios are described by the same petrological relations in field II (Fig. 3). But, while crossing (either up T or down T) reaction:

$$Atg = Fo + Tlc + H_2O \quad (2)$$

has a deep impact on associated ultramafic rocks, it has no influence on chromitite. The petrological relations of chromitite at lower temperature (field I of Fig. 3) are similar. For example, crossing reactions:

$$Dsp = Cm + H_2O \quad (3)$$

$$Atg + Brc = Fo + H_2O \quad (4)$$

has no influence in chromitite. In both fields I and II, the assemblage of full hydrated model chromitite is the same, Spl + Chl + Brc (except if hydration is not pervasive, allowing the effective bulk composition at the olivine reaction site to be strongly deviated towards olivine, as in the deep interior of the olivine grains, producing varied assemblages like Atg + Brc + Chl and Ol + Brc + Chl).

An analysis of the topological consequences of varying pressure and temperature at temperature higher than eq. 1 demonstrates that model chromitite has the spinel+olivine assemblage whatever the P–T condition is. That is, all the intervening reactions (grey coloured in Fig. 2) have no influence in model chromitite even above the terminal reaction:

$$Chl = Ol + En + Spl + H_2O, \quad (5)$$

that represents the maximum stability of chlorite (Fig. 2; Staudigel & Schreyer, 1977; Jenkins, 1981; Kempf *et al.*, 2022; Lakey & Hermann, 2022). Hence, that eq. 1 is the only reaction that affects chromitite has the foremost consequence of making the phase relations for this type of rock shown in Fig. 3 general at any isothermal-isobaric condition above and below eq. 1.

The relations shown in Fig. 3 deserve further detailed analysis. At the three isothermal conditions considered, model chromitite WR0 shows the same assemblage spinel+olivine in the absence of fluid infiltration (bottom panel, stage 1, Fig. 3). At this stage 1, no transformation is expected relative to the original magmatic assemblage (stage 0) except for Fe–Mg exchange between spinel and olivine (see below). Initial ingress of fluid in fields I and II (stage 2: transient H_2O subsaturation in Fig. 3) triggers the formation of chlorite and brucite, but olivine persists because H_2O saturation is not reached, leading to total consumption of H_2O. This translates into crosscutting tie-line relations (Spl–Ol–Chl–Brc) in the phase diagram projected from H_2O fluid (Fig. 3b and e), most of which are omitted for clarity. Upon continued fluid influx and completion of hydration in these two fields (Fig. 3c and f), olivine is exhausted and model chromitite is made of spinel, chlorite, brucite and fluid (stage 2). These transformations are accompanied by formation of new spinel composition relative to that of stages 0 and 1 (see below). For Ol-dominated rocks, like dunite, the corresponding assemblage would be Atg-Brc-Chl.

If balanced in the MASH system, eq. 1 takes the form:

$$5.5\ Mg_2SiO_4 + 2.5\ MgAl_2O_4 + 12\ H_2O = Mg_{9.5}Al_5Si_{5.5}O_{20}(OH)_{16}(Chl5.5) + 4\ Mg(OH)_2 \quad (6)$$

In this reaction, Chl5.5 is defined as $Mg_{9.5}Al_5Si_{5.5}O_{20}(OH)_{16}$, intermediate between end-members $Mg_{10}Al_4Si_6O_{20}(OH)_{16}$ and $Mg_9Al_6Si_5O_{20}(OH)_{16}$ (10-4-6 Chl–9-6-5 Chl; Spear, 1993), related by the tschermak exchange $Al_2Mg_{-1}Si_{-1}$. The stoichiometric coefficient ratio olivine/spinel of 5.5:2.5 in this reaction indicates that, upon full hydration of a spinel+olivine mixture dominated by spinel in fields I and II of Fig. 3, olivine is efficiently exhausted.

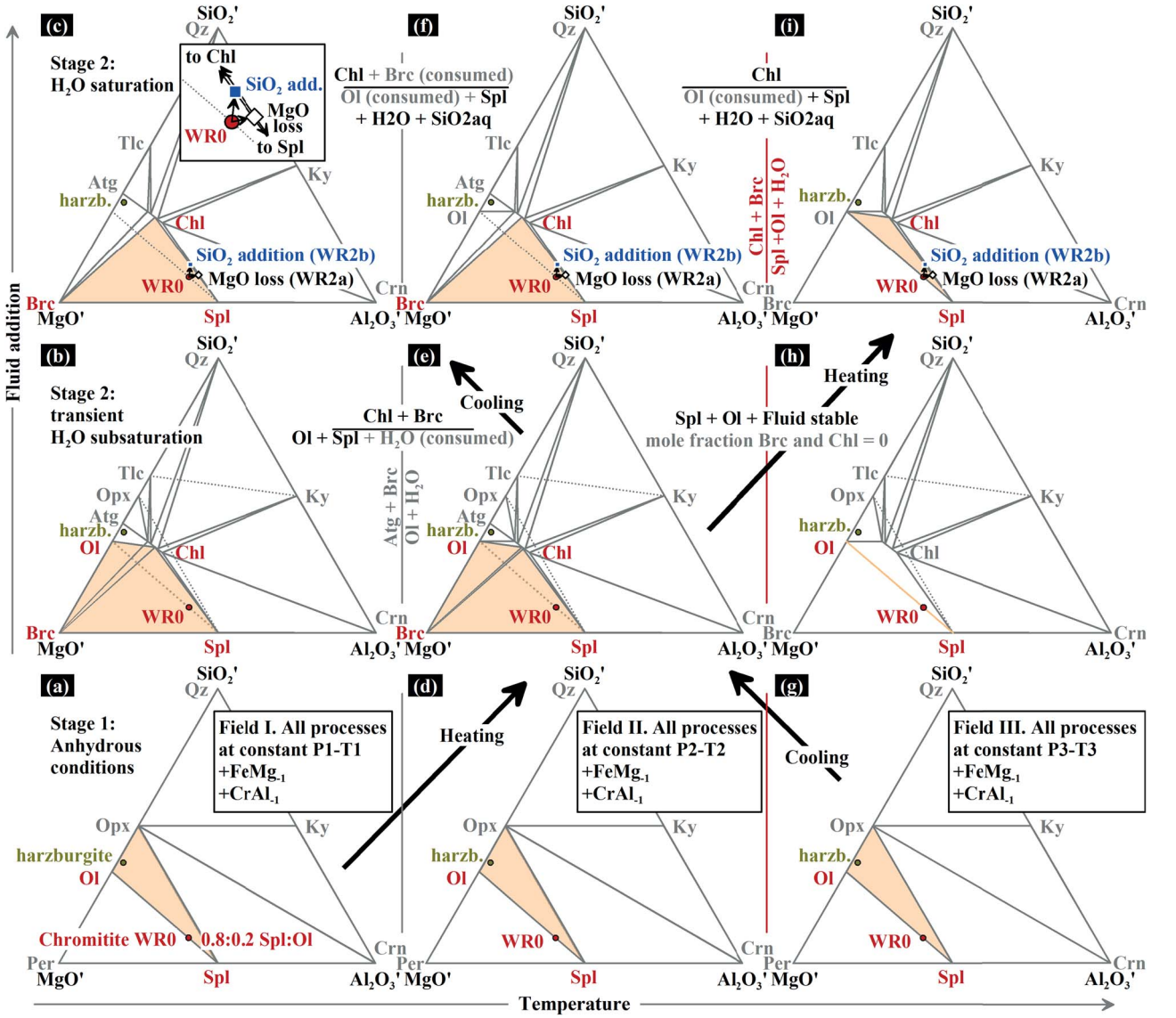

Fig. 3. Three vertical series of MgO'-Al_2O_3'-SiO_2' phase diagrams projected from H_2O and exchange vectors $FeMg_{-1}$ and $CrAl_{-1}$ in the FMACrSH system illustrating the response of anhydrous chromitite to H_2O-fluid infiltration at three nominally isothermal-isobaric conditions corresponding to fields I, II and III considered in Fig. 2. Spinel and olivine proportions in model chromitite are in molar units. A, B and C: Field I (below the stability of Ol + Fluid). D, E and F: Field II (below the stability of Chl + Brc) and F, G, H: field III (above the stability of Chl + Brc). The phase relations relevant and not relevant for chromitite transformation are red/orange and grey coloured, respectively. The chlorite solid solution is defined as $Mg_{10}Al_4Si_6O_{20}(OH)_{16}$ – $Mg_9Al_6Si_5O_{20}(OH)_{16}$ (10-4-6 Chl–9-6-5 Chl; Spear, 1993), related by the tschermak exchange $Al_2Mg_{-1}Si_{-1}$. Note that all isothermal-isobaric scenarios reach the same assemblage Spl + Chl upon hydration and the metasomatic effects of fluid-mediated MgO loss and/or silica addition (WR2a and WR2b, respectively; see inset in C), and that this assemblage is reached either upon heating or cooling (denoted by thick grey arrows). See text for details.

For example, infiltration of 12 moles of H_2O in a mineral assemblage with 6 moles of olivine and 24 moles of spinel (Ol/Spl ratio = 0.2:0.8; MASH system) will completely exhaust olivine leaving 19.5 moles of residual spinel (coexisting with 1 mole of chlorite and 4 moles of brucite). This straightforward consumption of olivine in this type of Ol-poor mineral assemblages would make impossible any further progress of reaction in a closed system. Hence, additional metasomatic processes are needed to trigger further transformation of residual spinel in fully hydrated (i.e. Ol-free) chromitite below eq. 1.

Open system

Olivine-present relations below eq. 1

Brucite is not generally present in olivine-lacking low-temperature assemblages of transformed chromitite, implying that it generally dissolves at fully-hydrated stage 2 (fields I and II in Figs 2 and 3) (Gervilla *et al.*, 2012; Klein *et al.*, 2020; Pujol-Solà *et al.*, 2020). Given mass-balance requirements (see section 'Mass-balance model' below), this is probably the result of fluid-mediated metasomatic processes that trigger what has been termed in the literature a) MgO loss out of the system or b) SiO_2 gain from external sources (e.g. Malvoisin, 2015; Colás *et al.*, 2017; and references therein). Any combination of these two processes can explain the lack of brucite below eq. 1, but we shall consider them as two model end-member processes for the moment.

In the diagrams of Fig. 3, MgO loss and SiO_2 addition are illustrated for WR0 by two vectors that drive bulk-rock shifts away from the MgO' apex and towards the SiO_2' apex, respectively, while Al_2O_3' may slightly increase (MgO loss) or decrease (SiO_2 gain). These shifts in bulk composition during stage 2 would

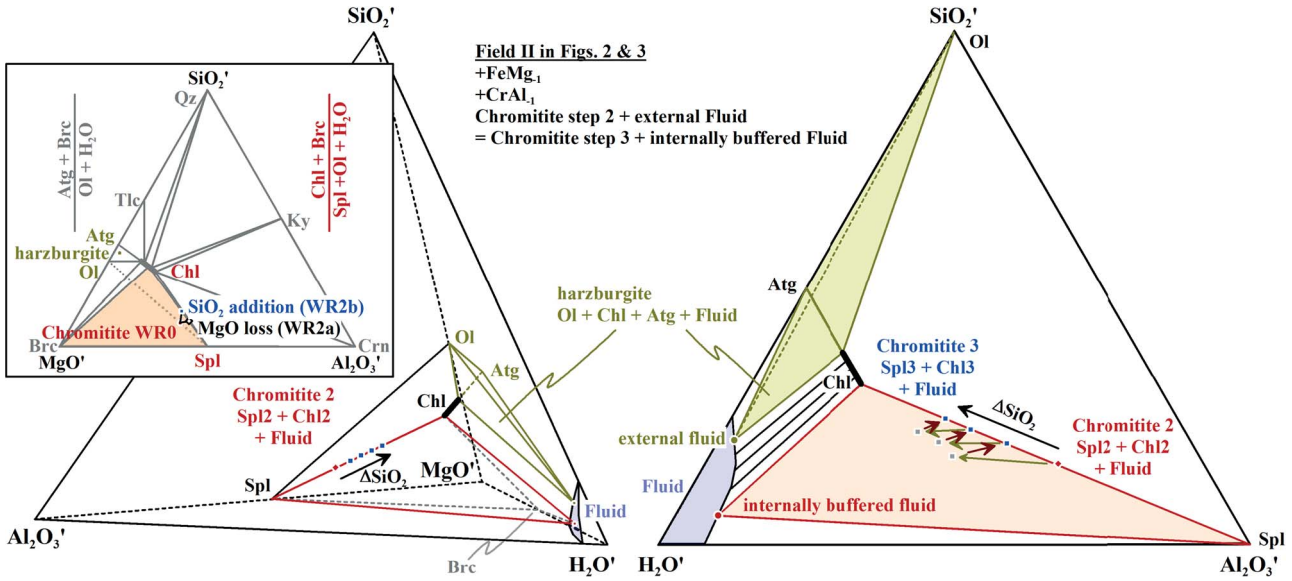

Fig. 4. Schematic phase relations for reaction of chromitite with multicomponent fluid fluxed from adjacent metaultramafic rocks in the FMACrSH system projected from exchange vectors $FeMg_{-1}$ and $CrAl_{-1}$. The diagrams correspond to P–T conditions of field II of Figs 2 and 3 under full hydrated conditions when brucite has been consumed in the chromitite assemblage during previous MgO-loss or SiO_2-gain metasomatic processes (Fig. 3f). The MgO′–Al_2O_3′–SiO_2′–H_2O′ tetrahedron depicts the shift in bulk composition of chromitite with Spl + Chl plus buffered fluid upon infiltration of external fluid buffered by Atg + Chl + Ol of adjacent serpentinitic rock. The triangular plot Al_2O_3′–SiO_2′–H_2O′ (neglecting MgO′) shows the reaction imperfectly but more visibly. See text for explanation.

eventually reach WR2a and WR2b, respectively, driving the brucite-chlorite-spinel assemblage to the chlorite-spinel tie-line (Fig. 3c and f). The end-member processes can be qualitatively described as:

$$Spl + Ol + H_2O = Chl + MgO^{aq}\ (MgO\ loss) \quad (7)$$

$$Spl + Ol + H_2O + SiO_2{}^{aq} = Chl\ (SiO_2\ gain) \quad (8)$$

(avoiding the intermediate brucite-forming step), leaving in both cases the solid assemblage spinel+chlorite upon exhaustion of olivine.

Both, MgO loss and SiO_2 addition may not necessarily end at the Chl-Spl tie-line, driving the system to develop quartz and/or talc and/or other Fe–Mg–Al–Cr–Si–H silicates and oxi-hydroxides. The general lack of these phases in chromitites indicates that the metasomatic process is more complex than implied in Fig. 3, as discussed below. However, the local presence of diaspore, corundum, cordierite, kyanite, andalusite and staurolite, considered continental crust-derived and exotic to the chromitite (Robinson *et al.*, 2015; Pujol-Solà *et al.*, 2021 and references therein), are perfectly possible upon metasomatism of chromitite. This important issue is, however, not developed in this contribution.

Olivine-absent relations below eq. 1

Once olivine is exhausted below eq. 1 and the spinel+chlorite assemblage has been developed by metasomatic processes, further reaction would apparently be not possible. However, metasomatism can trigger additional bulk compositional shifts and further reaction in the spinel+chlorite+fluid assemblage that result in continued dissolution-precipitation processes upon continued fluid infiltration. One of these dissolution-precipitation processes that is commonly proposed in the literature is the unconstrained (from a mass-balance perspective) preferential dissolution of component $MgAl_2O_4$ of spinel solid solution in a fluid (Gervilla *et al.*, 2012; Merinero *et al.*, 2014; Colás *et al.*, 2019). As described in the literature, this process implies dissolution of MgO and Al_2O_3 in equimolar amounts to form a new spinel of unrestricted composition upon continued dissolution, forming a continuous compositional trend from Mg-Al-richer towards Fe–Cr-richer spinel. However, there are some issues with this model. The dissolution of equimolar MgO and Al_2O_3 in spinel implies equimolar increments in FeO and·Cr_2O_3, making the process too ideal. From a thermodynamic and mass-balance perspective, it is certainly odd such a tight constraint. In fact, the comparison of the expected compositional changes during equimolar transformation of $MgAl_2O_4$-rich and $MgCr_2O_4$-rich primary mantle spinels invalidates this equimolar model. Thus, while stoichiometric constraints allow mantle $MgAl_2O_4$-rich spinel to potentially undergo equimolar transformation, the same constraints indicate that $MgCr_2O_4$-rich mantle spinel cannot. Thus, high MgO and Cr_2O_3 in the latter prevent extensive Cr–Al exchange towards Cr-richer composition while extensive Fe–Mg exchange towards Fe-richer compositions takes place (Gervilla *et al.*, 2012; Colás *et al.*, 2019 and references therein). Hence, the model of preferential dissolution of $MgAl_2O_4$ component in spinel during transformation does not seem to hold appropriate. In fact, we infer that the system should only rarely respond in such simple way to metasomatic processes. Instead, the system should respond as a whole via recrystallization and dissolution-precipitation processes involving all intervening solid and fluid solutions and not just by dissolution of $MgAl_2O_4$ component in spinel. This implies complex multicomponent reactions between multicomponent spinel, chlorite and externally-derived fluids that continuously shift bulk-rock, mineral and fluid compositions along multicomponent compositional vectors that are not necessarily constrained by the equimolar dissolution of MgO and Al_2O_3 in spinel. As demonstrated below in section ‘Mass-balance model’, the equimolar constraint in spinel is just one out of infinite possibilities of non-equimolar Al-Cr and Mg-Fe shifts in this mineral.

Interaction between spinel, chlorite and internal and external fluids is qualitatively shown in the tetrahedral and triangular

diagrams of Fig. 4. In this figure, the brucite-lacking chromitite assemblage spinel+chlorite (step 2) coexists with an internal fluid with composition buffered by the solid assemblage. The progressive infiltration of SiO_2-richer external fluid from nearby serpentinitic rocks that enclose mantle chromitite bodies, buffered by the corresponding antigorite+chlorite+olivine assemblage, drives reaction in fluxed chromitite (step 3) to restore the composition of the fluid towards the composition of the internally-buffered fluid. The transformation, described as:

$$\text{Chromitite step 2 (Spl2 + Chl2) + Fluid (external)} = \text{Chromitite step 3 (Spl3 + Chl3) + Fluid (internal)}, \quad (9)$$

involves changes in bulk-rock and mineral and fluid abundances, as shown in Fig. 4. For simple mass-balance requirements, the bulk composition of transformed chromitite shifts along the spinel+chlorite tie-line towards SiO_2-richer composition (Fig. 4). This reaction preserves the assemblage Spl + Chl of transformed chromitite while chlorite increases and spinel decreases progressively. These changes and the corresponding changes in mineral compositions are quantitatively explored below in section 'Mass-balance model'.

Olivine-present and -absent relations above eq. 1

At temperature higher than eq. 1 (field III, Figs 2 and 3), chromitite retains the original assemblage spinel+olivine coexisting with added fluid at stage 2 (Fig. 3h and i). Apparently, only changes in the Fe–Mg composition of these phases relative to previous stages 0 and 1 are expected at this stage. However, fluid-mediated metasomatic MgO-loss or SiO_2-gain processes like those attending fields I and II will drive model chromitite WR0 towards the same WR2a and WR2b (Fig. 3i). As in fields I and II, this process will exhaust olivine and develop the assemblage spinel+chlorite following the same qualitative eq. 7 and eq. 8. Once olivine is exhausted, the spinel+chlorite assemblage reacts, as illustrated in Fig. 4 for field II, with external SiO_2-richer (or MgO-poorer) infiltrating fluid evolved from nearby metaultramafic rocks, in this case buffered by assemblage Ol + Tlc + Chl (as in Fig. 3i) or, at higher temperature, by Ol + En + Chl (not shown but easily deduced from Fig. 2). The result of this interaction is the progressive shift of the bulk composition of model chromitite towards SiO_2-richer compositions, the consumption of some spinel and the formation of additional chlorite, and the change in composition of both phases during a progressive dissolution-precipitation process, in all aspects like lower temperature chromitites.

Hence, the same final assemblage spinel+chlorite is developed in model chromitite irrespective of temperature above or below eq. 1. Still, because of its persistent P–T stability, this assemblage would be developed in chromitite upon fluid infiltration and metasomatism not only in the three fields considered but at any temperature below the maximum stability of chlorite (ca. 800°C, eq. 5, Fig. 2), where the spinel+chlorite assemblage disappears and spinel+olivine+orthopyroxene forms. This conclusion holds for isothermal-isobaric conditions, cooling (for example, evolution from Fig. 3g through e to c) or heating (for example, from Fig. 3a through e to i), even if eq. 1 is crossed in one or the other direction. This peculiar behaviour of chromitite, derived from the persistence of spinel+chlorite stability in P–T space below ca. 800°C and the operation of metasomatic processes in this type of rock, adds to previous noticeable behaviour of model

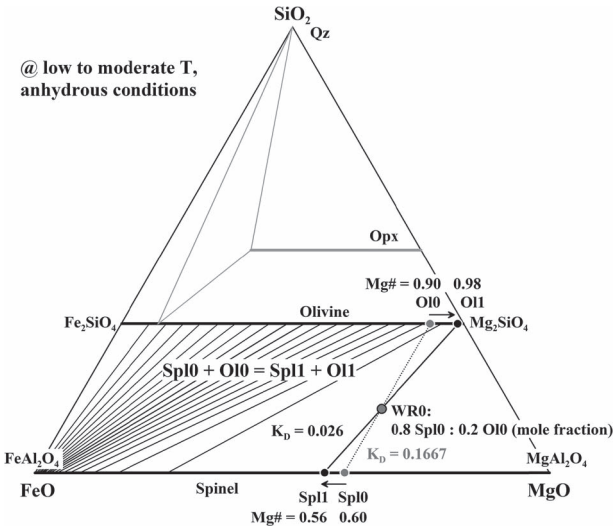

Fig. 5. Fe–Mg exchange between spinel and olivine in a closed system (eq. 10) at high T mantle conditions (grey symbols and dotted tie-line; $K_D = 1.667$) and moderate to low T in the absence of fluid (black symbols and tie-lines; $K_D = 0.026$). K_Ds are partition coefficients as defined in eq. 10. For reference, the calculated tie-lines for Fe–Mg partition among olivine and spinel at moderate to low T is shown for the whole range of mineral compositions. The phase relations involving orthopyroxene and quartz are schematic. Note mild compositional effects in spinel (Spl0 > Spl1) upon Fe–Mg exchange with olivine. See text for further explanation.

chromitite: the end-product of metasomatic processes during chromitite transformation at any isothermal-isobaric condition, upon cooling or upon heating below ca. 800°C is the assemblage spinel+chlorite.

This statement has significant implications for the interpretation of the temperature evolution of transformed chromitites. But, before we explore these implications using the textural-mineral composition evolution of natural rocks, an evaluation of the compositional changes in spinel and chlorite must be explored. Due to the lack of knowledge of the standard-state thermodynamic properties of end-members of Cr-chlorite, and of solid solutions models for Cr–Fe–Mg–Al chlorite, we follow below a mass-balance approach. The offered mass-balance approach is constrained by the common composition of minerals in natural primary and transformed chromitite in the FMACrSH system.

MASS-BALANCE MODEL

In what follows, no inferences on temperature or change in temperature during the analysed processes are attempted. However, it should be noted that, for simplicity, all mass-balances are considered to take place under isothermal-isobaric conditions within the stability of Brc + Chl (eq. 1) in Fig. 2.

Closed system except for H_2O

A model chromitite formed by 0.8 (molar units) of high-Al spinel (Cr# = 0.5 and Mg# = 0.6, Spl0) coexisting with 0.2 olivine (Mg# = 0.9, Ol0), both typical of a hot shallow mantle environment (>1200°C; ca. 0.3 GPa, ca. 10 km depth; Arai & Miura, 2016 and references therein), has the bulk composition 0.2 SiO_2, 0.4 Al_2O_3, 0.4 Cr_2O_3, 0.36 FeO, 0.84 MgO (molar units, WR0). For this initial model rock, the Fe–Mg partition coefficient (K_D) between spinel and

Table 1: Calculated composition of olivine and spinel (and orthopyroxene with 0 molar amount) in anhydrous model WR0 at 1200 and 400°C at 0.3 GPa

	T (°C)	Xmol	SiO_2	Al_2O_3	Cr_2O_3	FeO	MgO	XMg#
Ol	1200	0.2	1	0	0	0.267	1.733	0.867
Spl	1200	0.8	0	0.5	0.5	0.383	0.617	0.617
Opx	1200	0	1.833	0.138	0.029	0.226	1.607	0.877
Ol	400	0.2	1	0	0	0.128	1.872	0.936
Spl	400	0.8	0	0.5	0.5	0.418	0.582	0.582
Opx	400	0	1.964	0.025	0.011	0.148	1.816	0.925

olivine is 0.1667 (Fig. 5), as given by the equilibrium:

$$\begin{aligned} &Mg_2SiO_4(\text{forsterite}) + Fe(Cr,Al)_2O_4\ (\text{Fe-spinel}) \\ &= Fe_2SiO_4\ (\text{fayalite}) + Mg(Cr,Al)_2O_4\ (\text{Mg-spinel}).\ K_D \\ &= (X_{Fe}^{Ol} \cdot X_{Fe}^{Spl}). \end{aligned} \quad (10)$$

At any temperature below that of the indicated K_D in the absence of fluid, spinel-olivine couples would react following the Fe–Mg exchange of eq. 10 to the left, decreasing K_D eventually until olivine reaches ca. Mg# = 1 (near forsterite, making ca. $K_D = 0$) at appropriate low temperature. However, volume diffusion of Fe and Mg cations within the crystalline solids is low under low to moderate temperature conditions, which would normally hinder the progress of the exchange reaction (Fabriès, 1979; Engi, 1983; Lehmann, 1983).

Holding constant the bulk composition of model chromitite defined above (WR0), the composition of spinel for $Mg\#^{Ol} = 0.98$ (Ol1; e.g. Zhang *et al.*, 2019) is $Mg\#^{Spl} = 0.56$ (Spl1, $K_D = 0.026$; Fig. 5), while $Cr\#^{Spl}$ is kept constant at 0.5 due to the lack of Al-Cr exchange between spinel and olivine. This indicates that, even if kinetic barriers do not hamper reaction progress (see, for example, Zhang *et al.*, 2019), changes in spinel composition in model chromitite at low to moderate temperature are mild (maximum $\Delta Mg\#^{Spl} = -0.05$, if olivine would reach pure forsterite, and $\Delta Cr\#^{Spl} = 0$). Neither the molar abundances of the two phases are changed in the process (Fig. 5), nor, in practice, their volumes. For reference, the calculated compositions of coexisting olivine and spinel at 1200 and 400°C in anhydrous WR0 with software GeoPS (Xiang & Connolly, 2022), using the thermodynamic data and solution models indicated in section Methods, is given in Table 1. The software calculates an orthopyroxene-bearing assemblage, though the mole fraction of orthopyroxene is 0 in the whole P–T region because WR0 lies in the Ol–Spl tie-line of the Ol–Spl–Opx tie-triangle under anhydrous conditions (Fig. 3). The calculated compositions and associated $K_{DS}^{eq.\ 10}$ (0.248 and 0.095, at 1200 and 400°C, respectively) are within the range inferred above assuming ideal solid solutions (i.e. by means of mass-balance calculation) for model WR0, confirming mild compositional Mg-Fe effects in spinel composition at low to moderate T in the absence of kinetic barriers.

Upon the ingress of H_2O-fluid in model chromitite WR0, the net balance of eq. 1 and eq. 6 can be expressed as:

$$\begin{aligned} &27.5\ \text{WR0} + 12\ H_2O = 1\ \text{Chl5.5} + 4\ \text{Brc} + 19.5\ \text{Spl0} \\ &+ 1.25\ Cr_2O_3(Al_2O_3)_{-1} + 1.88\ \text{FeO}(\text{MgO})_{-1}, \end{aligned} \quad (11)$$

emphasizing the exhaustion of olivine. That the stoichiometric coefficients of the exchange vectors are non-zero in this mass-balance indicates that the process involves changes in the Fe–Mg and Cr–Al compositions of spinel, chlorite and brucite. Indeed, it is widely known that spinel suffers, in addition to partial consumption, variable extent of transformation towards higher Cr-Fe^{2+} and lower Al–Mg compositions during the dissolution-precipitation process, while newly formed chlorite is a Fe–Mg–Al–Cr solution strongly deviated towards Mg-Al compositions (Gervilla *et al.*, 2012 and references therein). Brucite should also be a Fe–Mg solution deviated to Mg-rich composition but, for simplicity, the chemical changes of spinel and associated chlorite are evaluated below assuming pure Mg-brucite.

The composition of spinel and chlorite are related by the following Fe–Mg and Cr–Al exchange reactions and associated K_{Ds}:

$$\begin{aligned} &\text{FeChl5.5} + \text{MgSpl} = \text{FeSpl} + \text{MgChl5.5}.\ K_D \\ &= (X_{Fe}^{Spl} \cdot X_{Mg}^{Chl5.5})/(X_{Mg}^{Spl} \cdot X_{Fe}^{Chl5.5}) \end{aligned} \quad (12)$$

and

$$\begin{aligned} &\text{CrChl5.5} + \text{AlSpl} = \text{CrSpl} + {}^{[VI]}\text{AlChl5.5}.\ K_D \\ &= (X_{Cr}^{Spl} \cdot X_{[VI]Al}^{Chl5.5})/(X_{Al}^{Spl} \cdot X_{Cr}^{Chl5.5}). \end{aligned} \quad (13)$$

In eq. 13, the Cr–Al exchange affects only the octahedral position of chlorite, whose composition is chosen to be intermediate in terms of tschermak exchange $(Fe,Mg)_{9.5}(Cr,Al)_5Si_{5.5}O_{20}(OH)_{16}$, with Si = 5.5 atoms per formula unit, hence termed Chl5.5 above. Mass-balance constraints allow calculating the composition of spinel fixing the compositions of the bulk rock WR0 and coexisting chlorite and pure brucite. In the calculations that follow, two chlorite formulas are considered: Mg-Al-rich, $Fe_{0.2}Mg_{9.3}Cr_{0.1}Al_{4.9}Si_{5.5}O_{20}(OH)_{16}$ (MgAlChl2), and Fe–Cr-rich, $Fe_{0.5}Mg_9Cr_1Al_4Si_{5.5}O_{20}(OH)_{16}$ (FeCrChl2), that represent reasonable Fe–Mg and Cr–Al compositions that allow considering the effect of chlorite composition in the shift in spinel composition in a closed system upon reaction progress.

For MgAlChl2, mass-balance in a closed system yields coexisting spinel Spl2 with Mg# = 0.5 and Cr# = 0.56, implying $K_{DFe-Mg}^{eq.\ 12} = 46.03$ and $K_{DCr-Al}^{eq.\ 13} = 30.74$ (Fig. 6a and b). Using FeCrChl2, the coexisting spinel Spl2 slightly increases Mg# (= 0.52) and decreases Cr# (= 0.54) relative to spinel coexisting with MgAlChl, with associated decreases in $K_{DFe-Mg}^{eq.\ 12}$ (= 16.75) and $K_{DCr-Al}^{eq.\ 13}$ (= 1.75, Fig. 6c and d). In both cases, the balance is:

$$27.5\ \text{WR0}\ (0.8\ \text{Spl0} + 0.2\ \text{Ol0}) + 12\ H_2O = 19.5\ \text{Spl2} + 1\ \text{Chl2} + 4\ \text{Brc} \quad (14)$$

or, converted to oxyequivalent units:

$$\begin{aligned} &1\ \text{WR0}\ (0.8\ \text{Spl0} + 0.2\ \text{Ol0}) + 0.11\ H_2O = 0.71\ \text{Spl2} \\ &+ 0.33\ \text{MgAlChl2} + 0.07\ \text{Brc} \end{aligned} \quad (15)$$

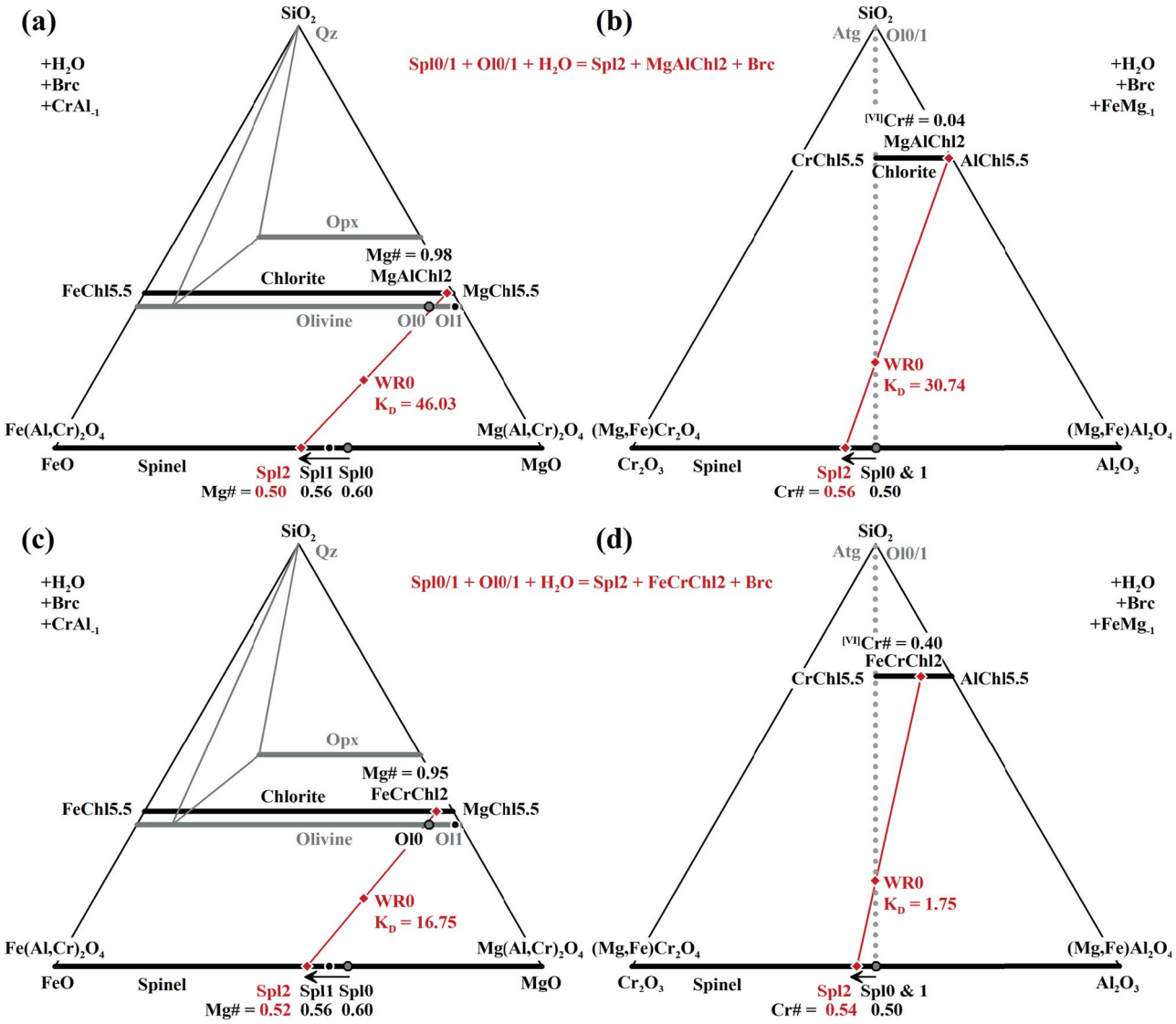

Fig. 6. FeO–MgO–SiO_2 and Cr_2O_3–Al_2O_3–SiO_2 diagrams illustrating the calculated compositions of spinel Spl2 coexisting with pure brucite and chlorite (a and b: MgAlChl2 $Fe_{0.2}Mg_{9.3}Cr_{0.1}Al_{4.9}Si_{5.5}O_{20}(OH)_{16}$; c and d: FeCrChl2 $Fe_{0.5}Mg_9Cr_1Al_4Si_{5.5}O_{20}(OH)_{16}$) in a closed system (WR0), and associated K_{Ds}. The compositions of initial and readjusted (eq. 10) spinel and olivine (Spl0, Ol0, Spl1 and Ol1) depicted in Fig. 5 are also shown. Note mild displacements towards Fe- and Cr-richer spinel compositions. See text for details.

to approximate the volume proportions of the solid phases. Figure 6a–d illustrates that, for a closed system (WR0) and with brucite present in the assemblage, whatever composition of chlorite in model chromitite yields a mass-balanced spinel slightly displaced towards Fe- and Cr-richer compositions relative to magmatic (Spl0) or Fe–Mg readjusted (Spl1) spinels. However, these compositions are far from those present in natural transformed chromitites, with much higher Fe and, in particular, Cr concentrations (e.g. González-Jiménez *et al.*, 2014; Zhou *et al.*, 2014; Arai & Miura, 2016). Hence, additional processes in an open system are needed.

Open system

Effects in brucite±olivine-present assemblages

Here we evaluate the consequences of two end-member simple metasomatic processes, MgO loss and SiO_2 addition, as described in section 'General petrologic model'. Below we show the effects of completion of metasomatic reactions in model WR0 after full-hydration stage 2 of Fig. 3c or f (i.e. from the closed system assemblage Spl2 + Chl2 + Brc described above) in terms of whole-rock composition, mineral abundance and mineral composition. However, it can be demonstrated, from a mass-balance perspective, that the same end-products are obtained if residual olivine is present in WR0 with Spl2 + Chl2 + Brc + Ol0/1 (i.e. after partial-hydration of Fig. 3b or e). For this reason, we describe the processes as stage 2a (MgO loss) and 2b (SiO_2 addition), to emphasize a continuous closed-to-open system during the consumption of olivine.

The disappearance of brucite from WR0 after full-hydration stage 2 by means of MgO loss yields the new bulk composition WR2a 0.27 SiO_2, 0.54 Al_2O_3, 0.54 Cr_2O_3, 0.48 FeO, 0.93 MgO, 0.39 H_2O (molar units). For this composition and assuming the composition of chlorite MgAlChl2 (see above), the reaction can be expressed as:

$$20.5\ \text{WR2a} = 19.5\ \text{Spl2a} + 1\ \text{MgAlChl2a (molar units)}, \quad (16)$$

or

$$1\ \text{WR2a} = 0.68\ \text{Spl2a} + 0.32\ \text{MgAChl2a (oxyequivalent units)}. \quad (17)$$

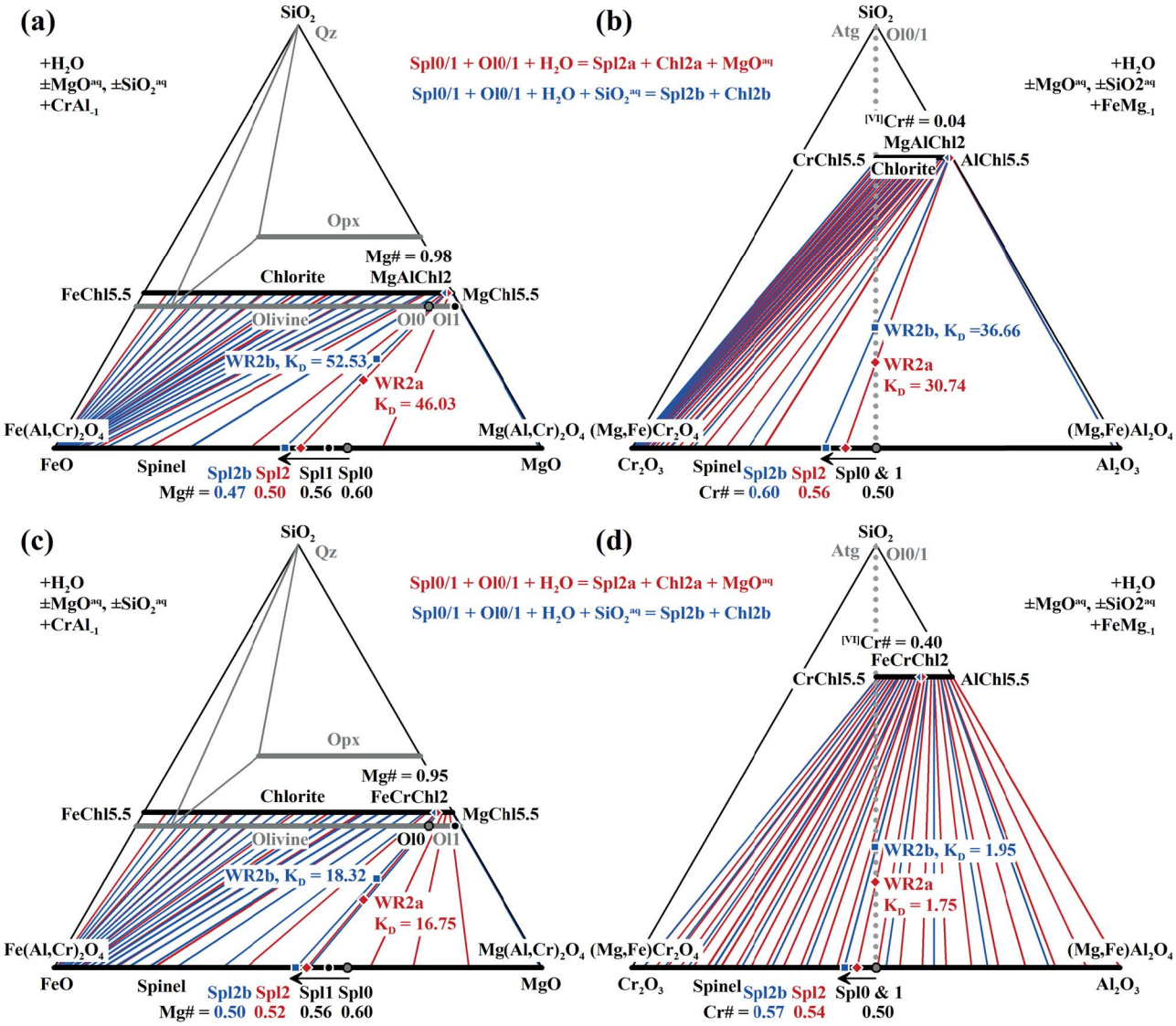

Fig. 7. FeO–MgO–SiO_2 and Cr_2O_3–Al_2O_3–SiO_2 diagrams illustrating the calculated compositions of spinel Spl2 coexisting with A and B: MgAlChl2 ($Fe_{0.2}Mg_{9.3}Cr_{0.1}Al_{4.9}Si_{5.5}O_{20}(OH)_{16}$) and C and D: FeCrChl2 ($Fe_{0.5}Mg_9Cr_1Al_4Si_{5.5}O_{20}(OH)_{16}$), and associated K_{Ds} for WR2a (MgO loss, reddish, collinear with WR0) and WR2b (silica addition, blue). The compositions of initial and readjusted (eq. 10) spinel and olivine (Spl0, Ol0, Spl1 and Ol1) are shown for reference. See text for details.

The same stoichiometric coefficients of spinel and chlorite in eq. 14 (closed system) and eq. 16 with and without brucite, respectively, implies the same calculated partition coefficients and compositions of Spl2a, as shown in Fig. 7a and b (red coloured lines and symbols; note that WR0 and WR2a are collinear in these plots). Similar calculations for MgO loss from WR0 using FeCrChl2 yield the same calculated reaction stoichiometries as in eq. 16 and eq. 17, and the same partition coefficients and compositions of Spl2a (Fig. 7c and d; red coloured lines and symbols).

However, the corresponding balances for SiO_2 addition (WR2b = 0.44 SiO_2, 0.56 Al_2O_3, 0.56 Cr_2O_3, 0.50 FeO, 1.18 MgO, 0.64 H_2O, molar units) are different:

$$12.5\ \text{WR2b}\ (0.51\ \text{Spl0} + 0.13\ \text{Ol0} + 0.29\ H_2O + 0.07\ SiO_2{}^{aq}) = 11.5\ \text{Spl2b} + 1\ \text{Chl2b (molar units)} \quad (18)$$

or

$$1\ \text{WR2b}\ (0.69\ \text{Spl0} + 0.17\ \text{Ol0} + 0.10\ H_2O\ SiO_2{}^{aq}) = 0.56\ \text{Spl2b} + 0.44\ \text{Chl2b (oxyequivalent units)}. \quad (19)$$

These balances, in particular eq. 19, illustrate that proportionally more chlorite is produced upon silica addition during stage 2 than during closed system (WR0) and MgO loss (WR2a) processes, as would be anticipated from simple topological relations (Fig. 3, inset). Furthermore, the calculated partition coefficients and compositions of Spl2b are also different (Fig. 7, blue coloured lines and symbols). For MgAlChl, spinel Spl2b has Mg# = 0.47 and Cr# = 0.60, with $K_{DFe-Mg}{}^{eq.\ 12} = 52.53$ and $K_{DCr-Al}{}^{eq.\ 13} = 36.66$ (Fig. 7a and b), while for FeCrChl, coexisting spinel increases slightly Mg# (= 0.50) and decreases Cr# (= 0.57) relative to Spl2a, and $K_{DFe-Mg}{}^{eq.\ 12}$ (= 18.30) and $K_{DCr-Al}{}^{eq.\ 13}$ (= 1.95) decrease (Fig. 7c and d).

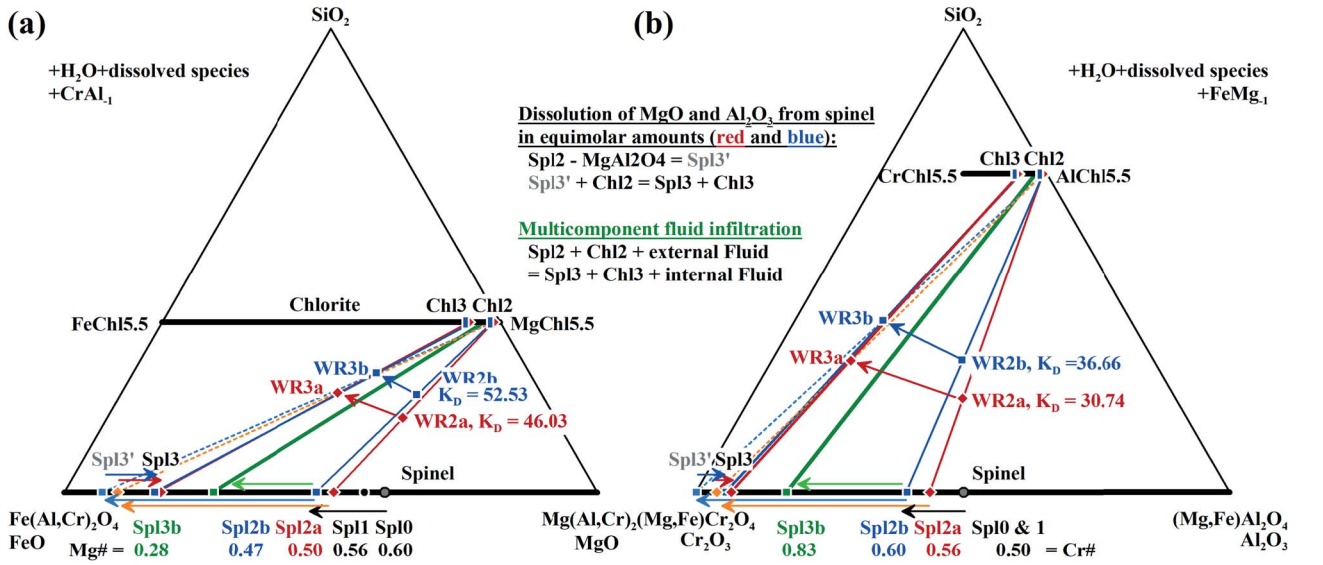

Fig. 8. FeO–MgO–SiO_2 and Cr_2O_3–Al_2O_3–SiO_2 diagrams illustrating the net consequences of unconstrained progressive dissolution of MgO and Al_2O_3 in equimolar amounts (= dissolution of $MgAl_2O_4$) from spinel solid solution (Spl2a and Spl2b) in WR2a (reddish) and WR2b (blue). Also shown is an intermediate step of formation of Spl3 (+Chl3, not shown for clarity) during infiltration of external fluid (green), as depicted in Fig. 4 and Table 2. See text for explanation.

In the balances above for WR2a using MgAlChl and FeCrChl, the total consumption of pre-hydration olivine (Ol0 or Ol1) of WR0 implies consumption of 11.36 oxyequivalent % of the initial spinel (Spl0 or Spl1) and 88.64 oxyequivalent% of initial spinel with the new calculated composition coexisting with chlorite (Spl2a in Fig. 7). The corresponding results for WR2b (silica addition) are similar, but spinel is consumed to a somewhat larger extent (17.86 oxyequivalent% of Spl0 or Spl1 consumed and 82.14 oxyequivalent% of initial spinel with readjusted composition Spl2b, Fig. 7c and b).

The similarity in the results of all calculations clearly indicates that total consumption of olivine/brucite from model WR0 after MgO loss or SiO_2 addition cannot produce new spinel compositions poor in Mg (e.g. Mg# = 0.2–0.3) and rich in Cr (e.g. Cr# = 0.8–09), as commonly observed in extensively transformed chromitites (Gervilla *et al.*, 2012 and references therein). The distributions of Chl-Spl tie-lines in Fig. 7 suggest that only WRs significantly displaced from model WR0 by means of metasomatic processes can account for such spinel compositions upon chromitite transformation.

Olivine-absent relations

Further metasomatic processes affecting Spl2-Chl2 after exhaustion of olivine and brucite are explored here. Because such metasomatic scenario ensues from previous ones, it can be safely assumed that it occurs at the same P–T condition. For this reason, $K_{DFe-Mg}^{eq.\ 12}$ and $K_{DCr-Al}^{eq.\ 13}$ calculated above will be applied.

The dissolution of spinel component ($MgAl_2O_4$) from spinel solid solution (see section "General petrologic model" above) is analysed in Fig. 8. In these diagrams, dissolution of spinel component from spinel solid solution implies deviation of spinel composition Spl2 from the MgO and Al_2O_3 apexes in equimolar amounts to form a new spinel of unrestricted composition, while the composition of chlorite Chl2 remains constant. This process is unconstrained by thermodynamic and mass-balance requirements (e.g. K_{Ds}). For example, unconstrained dissolution of 0.4 moles of $MgAl_2O_4$ from Spl2a calculated above ($Al_{0.9}Cr_{1.1}Fe_{0.5}Mg_{0.5}O_4$, stoichiometry rounded off to one digit) for WR2a transforms spinel into Spl3a' with composition $Al_{0.5}Cr_{1.5}Fe_{0.9}Mg_{0.1}O_4$. (Fig. 8). If the amount of dissolved $MgAl_2O_4$ is leached out of the dissolution-precipitation site, such a significant change in spinel composition would drive the system to a significantly different bulk composition. In Fig. 8, this shift in bulk composition is illustrated by WR3a, which is collinear with Spl3' and unreacted Chl2a. But this mineral couple is not in equilibrium at the isothermal-isobaric conditions of the implied $K_{Ds}^{Spl2a\text{-}Chl2a}$ ($K_{DFe-Mg}^{eq.\ 12} = 46.03$ and $K_{DCr-Al}^{eq.\ 13} = 30.74$), and the process triggers formation of a new Spl3a + Chl3a couple with compositions controlled by Fe–Mg and Cr–Al exchange reactions eq. 12 and eq. 13 to achieve equilibrium in WR3a (Fig. 8). Similar effects occur if 0.4 moles of $MgAl_2O_4$ dissolve from Sp2b calculated above for WR2b, driving the formation of Spl3b', Spl3b, Chl3b and shifting bulk composition to WR3b (Fig. 8). The two steps of the process can be described as:

$$\mathrm{Spl2} - \mathrm{MgAl_2O_4} = \mathrm{Spl3'}\ (\text{dissolution of } \mathrm{MgAl_2O_4} \text{ from Spl2, precipitation Spl3'}) \quad (20)$$

$$\mathrm{Spl3'} + \mathrm{Chl2} = \mathrm{Spl3} + \mathrm{Chl3}\ (\text{dissolution of Chl2 \& Spl3' and precipitation of Chl3 \& Spl3}) \quad (21)$$

In addition to being conceptually not appropriate due to the lack of justification for an equimolar dissolution of MgO and Al_2O_3 from spinel solid solution and the lack of restriction in the amount of $MgAl_2O_4$ dissolved (see section 'General petrologic model'), the above relations illustrate a rather complex and probably unnecessary process as far as the reaction progress must continuously generate transitional unstable spinel compositions previous to the formation of the stable ones at every intermediate step of spinel component dissolution.

A simpler and more constrained scenario is the transformation of chromitite by infiltration of a multicomponent external fluid, as qualitatively described in Fig. 4. In an open system characterized by loss and gain of matter, mass-balance

Table 2: Calculated composition of spinel, chlorite and whole-rock for an intermediate step 3 in the transformation of model chromitite shown in Fig. 8 (green symbols and lines)

	Xmol	Xoxy	Mg#	Cr#	SiO_2	Al_2O_3	Cr_2O_3	FeO	MgO	H_2O
Chl2b	0.08	0.44	0.98	0.04	5.50	2.45	0.05	0.20	9.30	8.00
Spl2b	0.92	0.56	0.47	0.60	0.00	0.40	0.60	0.53	0.47	0.00
WR2b	1.00	1.00	0.70	0.50	0.44	0.56	0.56	0.50	1.18	0.64
Chl3b	0.11	0.53	0.95	0.12	5.50	2.35	0.15	0.45	9.05	8.00
Spl3b	0.89	0.47	0.28	0.83	0.00	0.17	0.83	0.72	0.28	0.00
WR3b	1.00	1.00	0.64	0.65	0.61	0.41	0.76	0.69	1.24	0.88
ΔChl	0.03	0.09	−0.03	0.08	0.00	−0.10	0.10	0.25	−0.25	0.00
ΔSpl	−0.03	−0.09	−0.19	0.23	0.00	−0.23	0.23	0.19	−0.19	0.00
ΔWR	0.00	0.00	−0.06	0.15	0.17	−0.15	0.20	0.19	0.07	0.24

requirements are accounted for directly by changes in the composition of all intervening phases, with no intervening metastable transitional steps. The lack of knowledge of the composition of the fluid hampers proper calculations. We have overcome this issue by calculating spinel-chlorite pairs for stage 3 and, given a chlorite/spinel ratio, new bulk-compositions WR3. As an example, for a chlorite composition Chl3b as given in Table 2, using $K_{Ds}^{Spl2b\text{-}Chl2b}$ ($K_{DFe-Mg}^{eq.\ 12} = 52.53$ and $K_{DCr-Al}^{eq.\ 13} = 36.66$), the composition of Spl3b reaches Mg# = 0.28 and Cr# = 0.83 (Fig. 8, Table 2). This scenario has been constructed avoiding reaching very high-Cr and -Fe spinel such as above to make the plots of Fig. 8 readable. However, more deviated compositions can be reached upon slight modification of the composition of coexisting chlorite Chl3. On the other hand, increasing the chlorite/spinel molar ratio, as predicted in Fig. 4, to 0.11:0.89 (as opposed to 0.08:0.92 in stage 2, Table 2) translates into WR3b with higher SiO_2, Cr_2O_3, FeO, MgO and H_2O and lower Al_2O_3 than WR2b (Table 2). The model changes in bulk composition should be considered the result of fluid–rock interaction, but little can be inferred about the composition of the intervening internal and external fluids. However, it is consistent with the buffering capacity of the solid assemblage spinel-chlorite, which has not been changed in the calculations. These simple crude calculations illustrate that Cr- and Fe-rich spinel can be formed by metasomatism of transformed chromitite triggered by eq. 9 under isothermal-isobaric conditions (i.e. governed by constant $K_{Ds}^{Spl2b\text{-}Chl2b}$). It should be noted that a complete transformation of chromitite is not implied, and that this process should be inferred local, at reaction sites such as grain contacts and fractures and upon local dissolution-precipitation of the intervening phases, as commonly observed in natural transformed chromitites.

THERMODYNAMIC ISOBARIC T-X MODEL

As noted above, a reliable thermodynamic model cannot be constructed due to the lack of knowledge of the standard-state thermodynamic properties of Cr-chlorite end-members and of a Cr–Fe–Mg–Al chlorite solid solution model. However, we have constructed a temperature-bulk composition (T-X) diagram assuming that chlorite is a Fe–Mg–Al solid solution (Fig. 9). In this model, the change in bulk composition is from anhydrous WR0 through hydrous WR2b to hydrous WR3b. Even if imprecise, the model shows that a) the Spl + Chl + Fluid assemblage can be developed under isothermal-isobaric conditions and upon heating and cooling and b) Cr-rich composition of spinel is not necessarily indicative of lower temperature. Indeed, increasing Cr# in spinel is a strong function of spinel volume reduction and not temperature (or pressure). This is a necessary mass-balance requirement in a thermodynamic model constructed with spinel and, to a much lesser extent, orthopyroxene, as the only chromium-fractionating phases. But these predictions would also apply to the natural rocks composed of spinel and chlorite provided that the latter do not significatively partitions chromium. Hence, for a given bulk composition, Cr-rich spinel is expected whenever a decrease in its amount takes place either at isobaric-isothermal conditions or upon heating or cooling.

IMPLICATIONS

Assuming isothermal-isobaric conditions in the model presented here is the consequence of considering a single pulsed event of fluid infiltration into chromitite. This event would drive dissolution-precipitation of spinel straightaway during olivine consumption and brucite production. Once brucite and eventual residual olivine are exhausted, dissolution-precipitation of spinel and chlorite takes place. The model above considers sequential reaction processes at temperature below eq. 1 (Fig. 2). These processes necessarily involve changes in bulk composition triggered by infiltration of external fluid during the hydration processes. Otherwise, the assemblage spinel+chlorite without brucite would not be reached. But, because of the persistence of the spinel-chlorite assemblage in P–T space (Figs 2, 3 and 9), the same spinel+chlorite assemblage would be reached at temperature higher than eq. 1 in the absence of brucite, provided that external fluid continuously fluxed chromitite and the stabilities of orthopyroxene and olivine are not reached. Thus, above eq. 1, Spl1–Ol1 may have formed at anhydrous conditions due to Fe–Mg exchange, Spl2–Chl2 may have formed upon infiltration of Si-enriched external fluid and consumption of olivine, and Spl3–Chl3 may have formed once olivine was exhausted upon continued infiltration of external fluid, in all aspects like below eq. 1, except for the initial formation of brucite (Fig. 3).

Non-constant P–T conditions can be anticipated in the natural case (Figs 1 and 2) but, in general, either prograde or retrograde changes in P–T should not be considered the unique driving force for transformation. Instead, the key driving force is metasomatism. As demonstrated above using simple mass-balance and thermodynamic approaches, the extreme Fe–Cr-rich compositions of spinel in transformed chromitites cannot be reached in a closed system scenario. Metasomatic changes in bulk composition (at reaction sites) are needed to achieve them. The general full-hydration state of transformed chromitites without olivine,

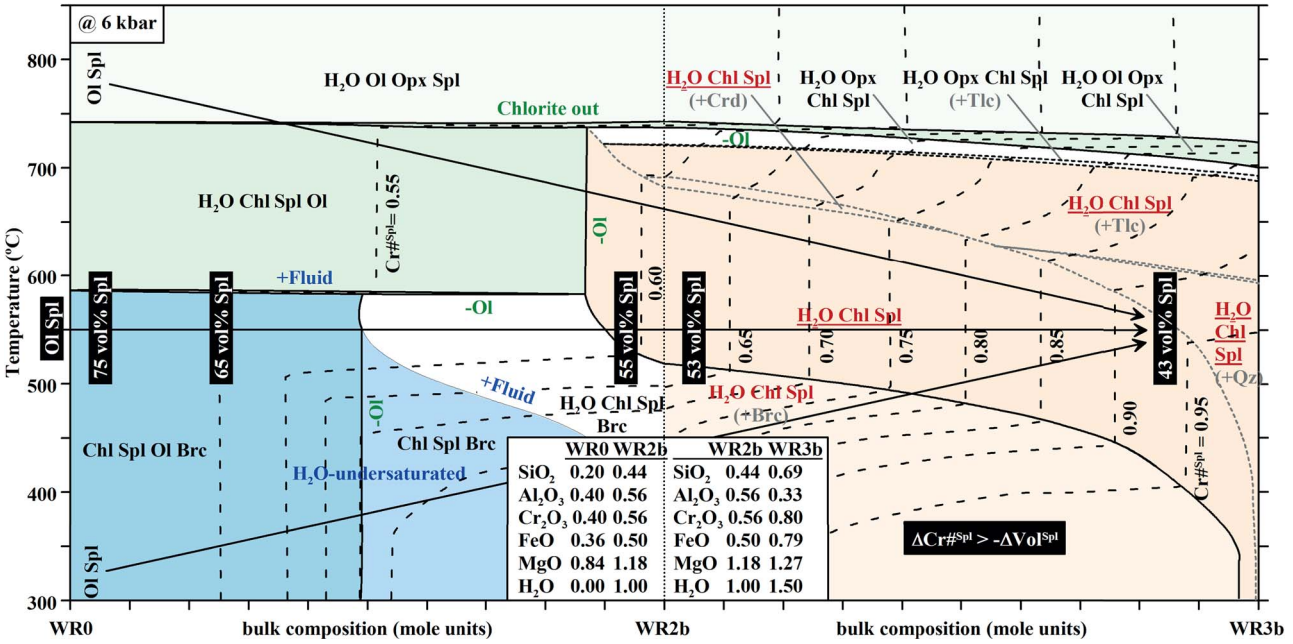

Fig. 9. Thermodynamic model for chromitite transformation in the FMACrSH system from anhydrous WR0 to fully hydrated WR2b and WR3b (mole units) at 0.6 GPa. Isopleths of Cr# in spinel are indicated. Isopleths of volume% spinel are not offered for clarity, but a few values given along the isobaric-isothermal transformation process demonstrate that increasing Cr# in spinel is strongly controlled by decreasing spinel volume and not necessarily decreasing temperature. The occurrence of cordierite-, talc- and quartz-bearing Spl + Chl fields are not expected for bulk compositions along WR2b-WR3b (i.e. within the 5-variant assemblage H_2O-Chl-Spl in the FMACrSH system, Figs 3 and 4), but they locally appear in the T-X diagram due to a) mass-balance constraints in stoichiometric bulk compositions calculated as mixtures of spinel and chlorite with Si content fixed at 5.5 atoms per formula unit (i.e. fixed tschermak exchange) and b) complexities in solid solutions, particularly chlorite. This mass-balance issue is illustrated by the low calculated abundances of cordierite, talc and quartz in their respective Spl + Chl fields (ranging 0–1.5 for talc, 0–0.13 for cordierite, and 0–0.3 for quartz, volume% of the solid assemblages). The H_2O–Chl–Spl–Brc field is split in two because brucite is nominally absent at any temperature upon reaching WR2b (SiO_2 addition) and beyond. Its presence is in part due to the effects of the complex solid solution of chlorite. For these reasons, the reddish fields highlight the predicted large stability of the spinel+chlorite+fluid assemblage once reached by original spinel+olivine mixtures upon metasomatism. Note that increase (dissolution) or decrease (growth) of $Spl^{Cr\#}$ can be triggered upon isochemical cooling or heating, respectively, once a given spinel+chlorite assemblage has been achieved.

as eventually opposed to less extended hydration in adjacent metaultramafic rocks that may contain relict mantle olivine, is a consequence of large spinel/olivine ratio (e.g. 0.8:0.2 molar, as modelled here) and the stoichiometric coefficient of olivine greater than spinel in eq. 6. Metasomatism has been recognized as a key process during cooling of chromitite (Colás *et al.*, 2017), but we here propose that progressive fluid infiltration of an external fluid in disequilibrium with chromitite produces, irrespective of P–T conditions and path, progressive textural-mineral changes by means of sequential dissolution of spinel Spl0 and Spl1, precipitation of Spl2, dissolution of Spl2 and precipitation of Spl3, as depicted in the general model for chromitite transformation of Fig. 10.

Regardless of the (eventual, for kinetic reasons) Fe–Mg exchange between spinel and olivine under anhydrous conditions (i.e. development of Spl1 + Ol1), our model is divided into two main hydration scenarios, with and without olivine (Fig. 10). In the first one, consumption of olivine is the major drive for transformation if H_2O-fluid is available. For thermodynamic (strong overstepping relative to the mantle assemblage/conditions) and mass-balance (large spinel/olivine ratio in chromitite coupled with stoichiometric coefficient of olivine greater than spinel in eq. 6) constrains, olivine consumes rapidly in this scenario. This process should hence drive a rapid change in the modal amounts of the new phases and in the textural development of the new assemblage. The end product of this step is Spl2, with a composition not much deviated from Spl0/Spl1, low-Cr chlorite Chl2 and a distinctive texture involving replacements of Spl0/Spl1 by Spl2 and Chl2. Once olivine is exhausted, the second step follows without interruption at isobaric-isothermal conditions or upon heating or cooling. In an olivine-lacking system where the Spl2-Chl2 assemblage is close to equilibrium, the composition of the infiltrating external fluid is the major drive for reaction. Not-so-overstepped P–T conditions (if any) relative to the previous step, coupled or not with relatively slow fluid flow, should drive slow changes in the mineral-textural development of transformed chromitite in this scenario. Likely, direct dissolution of Spl2-Chl2 in the fluid and precipitation of Cr-richer Spl3-Chl3 trigger formation of not-replacement textures.

All the mass-balance and thermodynamic reasoning and calculations above are strictly applicable to varied original mixtures of spinel and olivine, including high-Cr chromitites (Fig. 10). Decreasing the Spl/Ol ratio would simply produce more Spl2 of intermediate composition and, depending on the fluid flux, olivine may not be completely consumed, hampering development of spinel Spl3 with extreme Cr-rich composition except in local reaction domains/sites devoid of olivine. In high-Cr chromitites with spinel Spl0 reaching Cr# = 0.8 (but with similar Mg#), the Fe–Mg and Cr–Al reactions would proceed at a time, but the difference in Cr# of spinel Spl0, Spl2 and Spl3 would be minor while the dissolution-precipitation process will still produce Fe-rich spinel Spl3 (Fig. 10). General calculations are hence not applicable to chromitite of varied composition, and each specific case needs of appropriate calculations following the presented approach to arrive to conclusions regarding the physical–chemical factors controlling the transformation of chromitite.

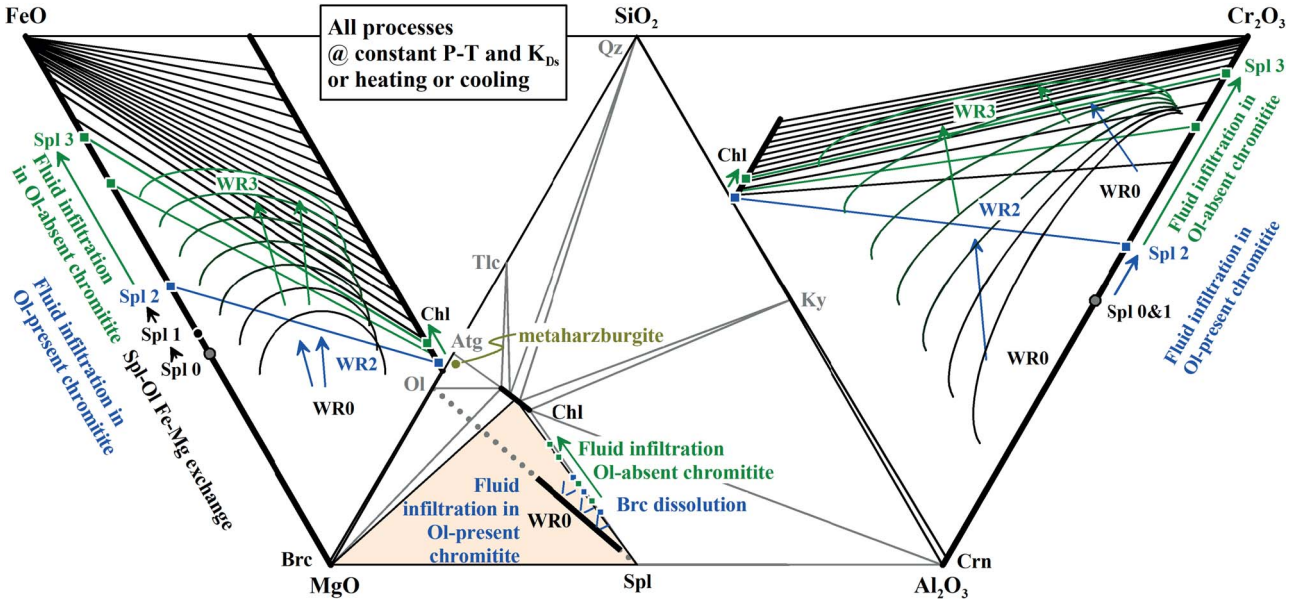

Fig. 10. General conceptual model for the transformation of chromitite of varied Spl + Ol composition through Cr-poorer to Cr-richer Spl + Chl mixtures. See text for explanation.

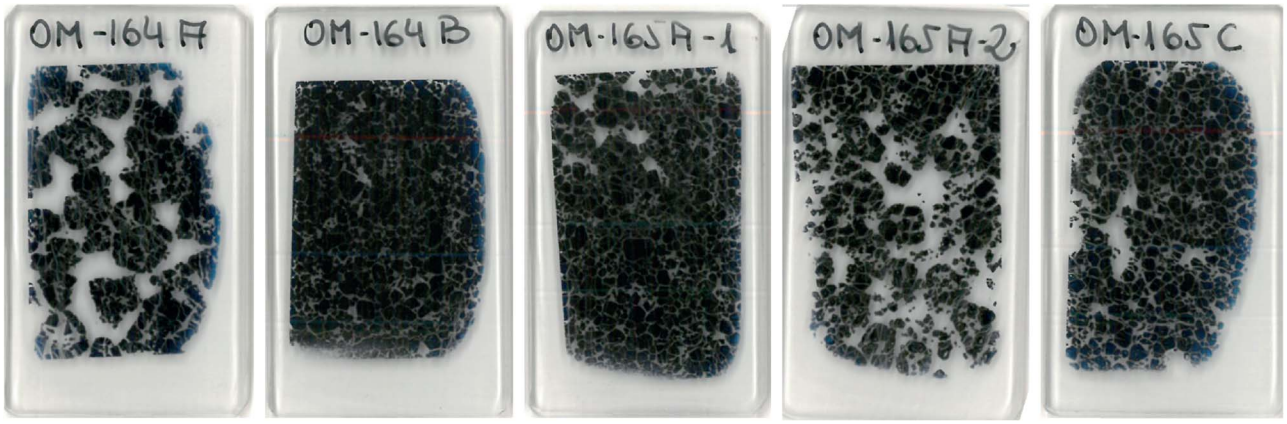

Fig. 11. Studied polished thin sections (26 mm x 46 mm) of massive and semi-massive chromitite samples from the Calzadilla metaophiolite.

The modelled textural-mineral transformation of chromitite ($Cr\#^{Spl}$ increases and $Mg\#^{Spl}$ decreases) is universal, and commonly interpreted in the literature as developed progressively during cooling both in the shallow oceanic environment and in the deep subduction and collision contexts (e.g. Gervilla *et al.*, 2012; Merinero *et al.*, 2014; Colás *et al.*, 2017, 2019; Fig. 1). For the same reasons given above that support that transformation of chromitite can proceed at temperature above eq. 1, prograde metamorphism below or above this reaction, crossing it or not, permits the same mineral-textural development and reaching high Cr-spinel+chlorite produced by precipitation of dissolved Cr-poorer spinel+chlorite. In short, the strong overstepping of the intervening mantle spinel+olivine assemblage coupled with infiltration of external fluid andmetasomatism does necessarily yield the same spinel+chlorite assemblage and mineral composition (at <800°C). However, once a given spinel+chlorite assemblage is reached, either upon retrogression or progression, further eventual cooling or heating under isochemical conditions would drive the growth of new spinel with increasing or decreasing Cr#, respectively (Fig. 9), as observed in cases of post-retrogression thermal metamorphism (González-Jiménez *et al.*, 2015).

APPLICATION: THE CALZADILLA METAOPHIOLITE

Geological and petrological settings

The Ossa-Morena Complex of the Variscan Iberian Massif contains, among other allochthonous units, remnants of a Cadomian volcanic arc and associated ophiolites, including the 602 Ma Calzadilla ophiolite formed in a supra-subduction setting (Arriola *et al.*, 1984; Aguayo Fernández, 1985; Jiménez-Díaz, 2008; Jiménez-Díaz *et al.*, 2009; Arenas *et al.*, 2018; Díez Fernández *et al.*, 2019; Arenas *et al.*, 2024; Novo-Fernández *et al.*, 2024). The crustal section of the ophiolite has suffered regional prograde dynamothermal metamorphism that reached amphibolite facies (525–575°C and ~0.5 GPa, ca. 15 km depth) during the Cadomian orogenic cycle at 540 Ma (Arenas *et al.*, 2018; Arenas *et al.*, 2024; Novo-Fernández *et al.*, 2024). A barrovian metamorphic gradient of ca. 30°C/km denotes a tectonic environment of collision and crustal thickening, in accordance with growth zoning in amphiboles of the amphibolites that denotes increasing metamorphic grade (Novo-Fernández *et al.*, 2024). The hydration of the basaltic rocks in the amphibolite facies is almost complete, with very scarce relics of clinopyroxene. Textural and phase relations

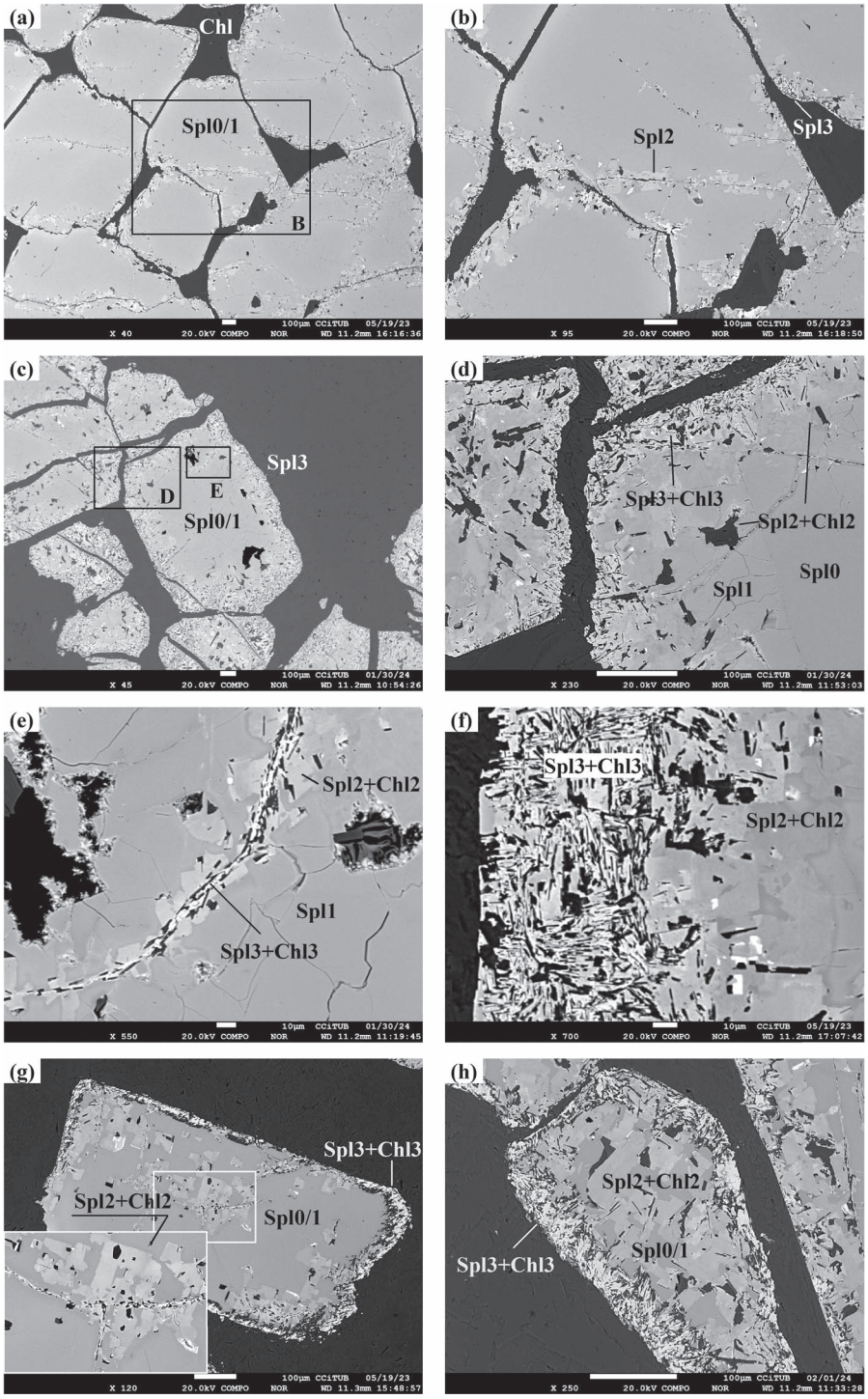

Fig. 12. Backscattered electron images of textural features of spinel (Spl, brighter) and chlorite (Chl, darker). The brighter shades of grey in spinel denote higher chromium and iron content. A: Slightly transformed grains of spinel surrounded by chlorite. Blocky blastic texture develops at the rims of grains and along fractures that locally cut across grains (arrows). The square denotes detailed portrait B. B: Detail showing blocky blastic spinel at the rims and along fractures. Note the very local development of bright spinel at some rims. C: Slightly transformed grains of spinel surrounded by chlorite. The squares denote detailed portraits D and E. D: Transformed rim of spinel. Towards the interior, blocky blastic spinel develops a chessboard-like texture associated with larger chlorite grains that denote recrystallization. The amount of chlorite decreases toward the preserved core devoid of inclusions. E: Detail of blastic spinel along fracture zone associated with near-idioblastic fine-grained chlorite. F: Detail of spinel rim where the chessboard-like blastic texture gradually changes towards a fine-grained intergrowth of brighter (Cr-richer) spinel and chlorite. G: Chessboard texture grading towards Cr-richer spinel associated with chlorite that concentrates at the core-rim transition (inset shows enlarged detail). H: Strongly transformed spinel grain with a chessboard core and fine-grained rims. The amount of chlorite decreases towards the core.

indicate that hydration took place during the collision event, when the ophiolitic slices were emplaced on top of, and within, the metasedimentary country rocks (the Serie Negra Group; Díez Fernández *et al.*, 2019; Novo-Fernández *et al.*, 2024). The strongly residual character of the harzburgites of the mantle section (up to 16% melt fraction extracted) has been also related to a forearc

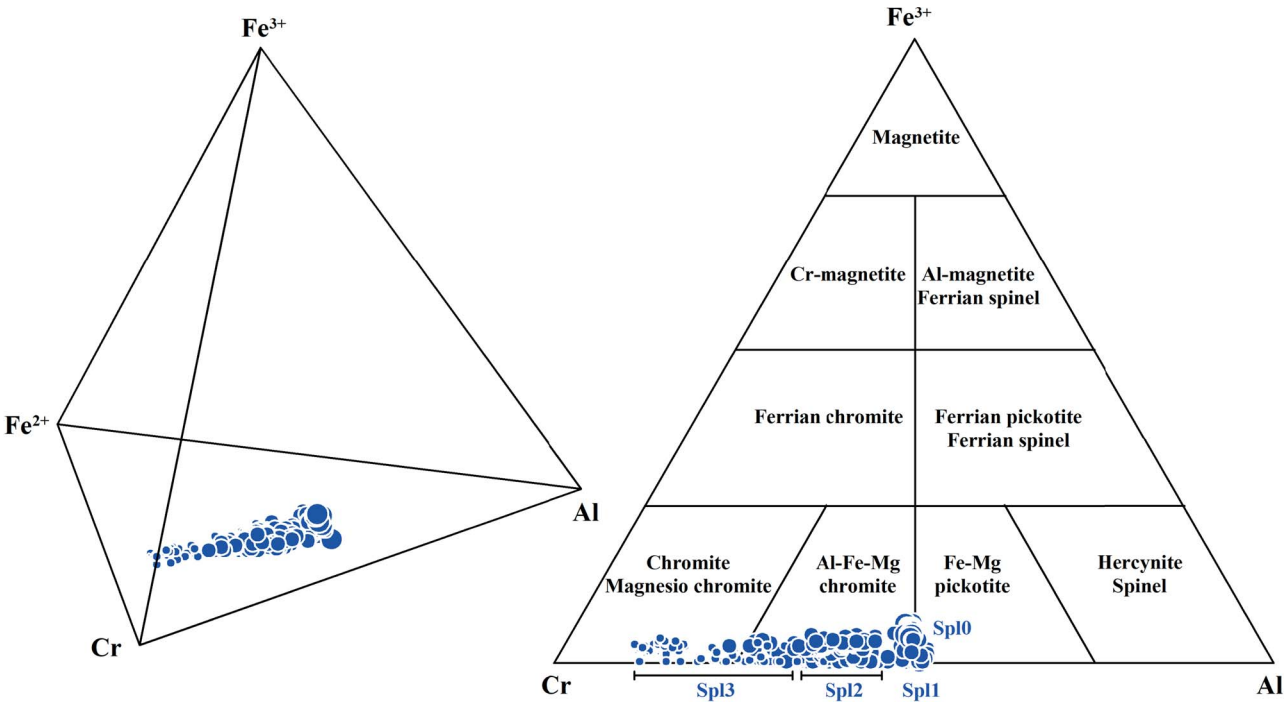

Fig. 13. Fe^{3+} content calculated by stoichiometry and classification of spinel (624 point analyses from the five samples illustrated in Fig. 11). The size of the symbols is proportional to Mg# (ranging 0.22–0.70).

environment (Novo-Fernández *et al.*, 2024). Peak metamorphic conditions in the metaperidotites and amphibolites are similar, suggesting a similar prograde evolution of the metaperidotites within the stability of antigorite and below the stability of olivine during the thickening event (Novo-Fernández *et al.*, 2024). The metaperidotites are almost completely serpentinized, with very scarce relicts of primary olivine and spinel. Even if hydration of the metaophiolite may have started during the forearc stage, phase relations indicate near-full hydration during prograde metamorphism.

The mantle section hosts several bodies of podiform chromitite. The primary magmatic composition of spinel from chromitite points to formation by forearc basalts (Merinero *et al.*, 2013, 2014; Novo-Fernández *et al.*, 2024). The chromitites are fully hydrated and essentially made of spinel and chlorite. Relics of olivine have not been reported (Aguayo Fernández, 1985; Merinero *et al.*, 2013, 2014; Novo-Fernández *et al.*, 2024). Spinel grains are partly replaced by chlorite and show varied compositions thought to have developed sequentially during cooling after peak-metamorphic conditions.

Samples

Samples were taken from the chromitite pods located close to El Cuco country house (Merinero *et al.*, 2014; Novo-Fernández *et al.*, 2024). They correspond to massive to semi-massive chromitites with interstitial chlorite (Fig. 11). Relics of olivine are not present and a few spinel grains contain inclusions of sulphides, calcic amphibole and phlogopite (see also Merinero *et al.*, 2013).

Textures and mineral composition

Hereafter we follow the terminology used above for different steps in the textural-mineralogical development of transformed model chromitite.

Spinel

Spinel grains appear systematically texturally and chemically zoned. Four types of spinel (Spl0, Spl1, Spl2 and Spl3) are distinguished based on their textural-compositional characteristics (Fig. 12). All these types exhibit very low to negligible Fe^{3+} content, as determined by stoichiometric calculations (Fig. 13). The cores (Spl0) are rich in Mg and Al, typical of preserved primary mantle spinel, with Cr# ca. 0.5 and Mg# ca. = 0.6 (Figs 14–17). Adjacent to the cores, development of wide diffuse regions of modified spinel (Spl1) commonly occur. This type of spinel is not associated with chlorite. It shows a composition similar to that of the primary cores in terms of Cr# but Mg# (ca. 0.5) and Fe^{3+} are slightly lower. Within and surrounding the cores and along fractures, recrystallized regions of spinel (Spl2) develop. XR maps and BSE images show that these recrystallized regions are in fact discrete blasts of blocky spinel with a chessboard-like texture of idioblastic Spl2 within Spl0/1 (best seen in the cores of grains of Fig. 12g and h). The individual grains are relatively coarse-grained (several tens up to >100 μm; Figs 12, 14–17). Systematically, this type of spinel is associated with relatively coarse-grained chlorite. The cores of Spl0 and Spl1 may be almost consumed by Spl2 in the more intensely transformed grains (Figs 12h and 17). The composition of this type of spinel is relatively constant, clustering around Cr# = 0.6 and Mg# ranging 0.5–0.6. Finally, fine-grained Fe–Cr-richer spinel (Spl3) develops at the rims and along fractures. Detailed textural analysis demonstrates that this development is texturally and chemically abrupt (e.g. Fig. 12e, f, g), involving the dissolution of Spl0/1 and Spl2 and a sudden increase in Cr# up to 0.8 to 0.9 and a decrease in Mg# down to 0.4 to 0.2 (Figs 14–17). Delicate pathways of reaction progress, like fractures, suggest that Spl3 development just followed Spl2 without a time gap in between (Fig. 12b and e). This type of spinel is set in a fine-grained texture intimately associated with fine-grained chlorite Chl3 (see below). The textural analysis suggests a dissolution-precipitation process in the formation of Spl3 + Chl3

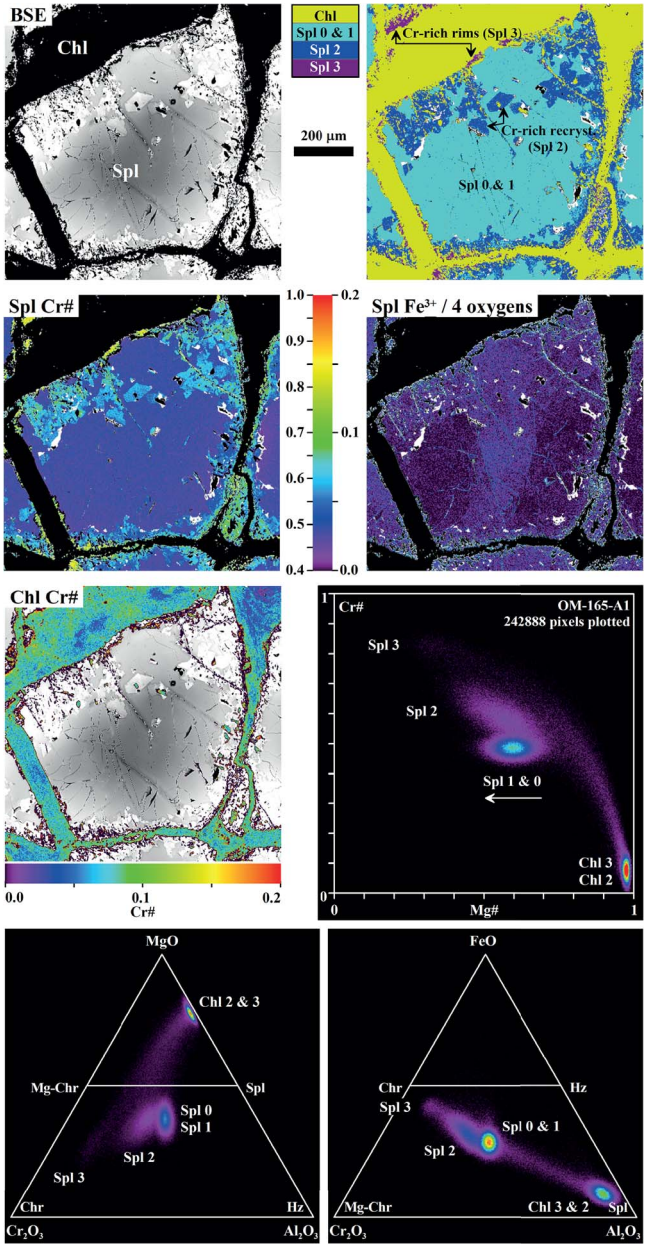

Fig. 14. Textural-chemical details of spinel and chlorite of sample OM-165-A1. From top to bottom and left to right: Back-scattered electron image highlighting shades of grey in spinel (Spl) driving chlorite (Chl) to black shade, phase-map generated after manipulation of XR images, Cr# and Fe^{3+} per formula unit in spinel, Cr# in chlorite, Cr# vs Mg#, MgO–Cr_2O_3–Al_2O_3 and FeO–Cr_2O_3–Al_2O_3 plots (molar units) in spinel and chlorite extracted from XR maps. Note mixed Spl–Chl pixels in the bivariate and triangular plots.

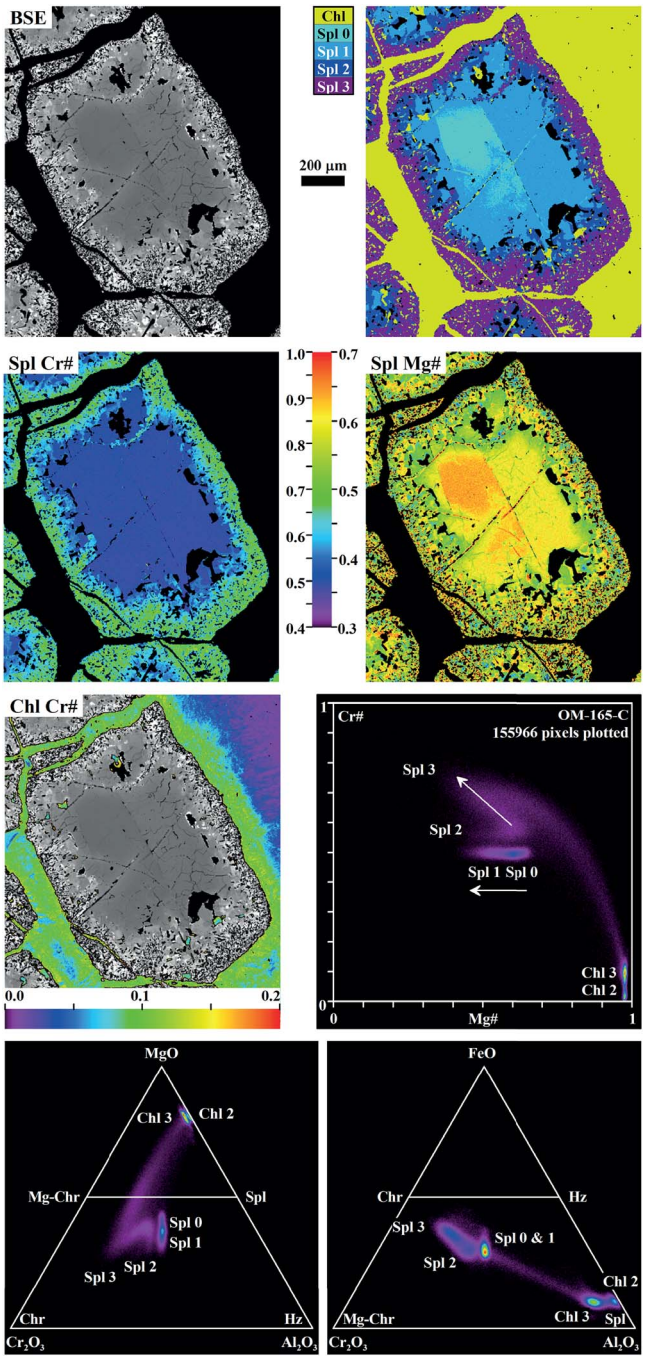

Fig. 15. Textural-chemical details of spinel and chlorite of sample OM-165-A2. All images and plots as in Fig. 14.

intergrowths radically different from the dissolution of Spl0/1 and replacement by Spl2 + Chl2.

Chlorite

Chlorite is Mg-rich, with Mg# = 0.95–0.98 but more variable in terms of Cr# that ranges from 0.02 to 0.14 (considering $^{[IV]}Al + {}^{[VI]}Al$). The highest Cr contents are 0.7 atoms per formula unit (20 O and 16 OH), which correlates negatively with Si and positively with Fe, implying Cr-Mg-tschermak substitution (Cr_2Si_{-1} Mg_{-1}; Fig. 18). The grains of chlorite Chl2 associated with Spl2 within spinel grains are richer in Mg-Al, clearly evidenced in cases of extensive replacement of Spl1/0 (Fig. 17), while the tiny crystals of Chl3 intergrown with Spl3 are richer in Fe–Cr (Figs 14–17). Grains of chlorite formed at this stage may however be relatively rich in Fe–Cr compared to typical Chl2 because of transformation during formation of Spl3 + Chl3 (Figs 15 and 16). Aggregates of chlorite in the matrix close to and away from the rims of spinel grains have composition of Chl3 and Chl2, respectively.

Bulk composition

Bulk compositions estimated from the XR maps are variable as a function of the surface proportions of spinel and chlorite. Thus,

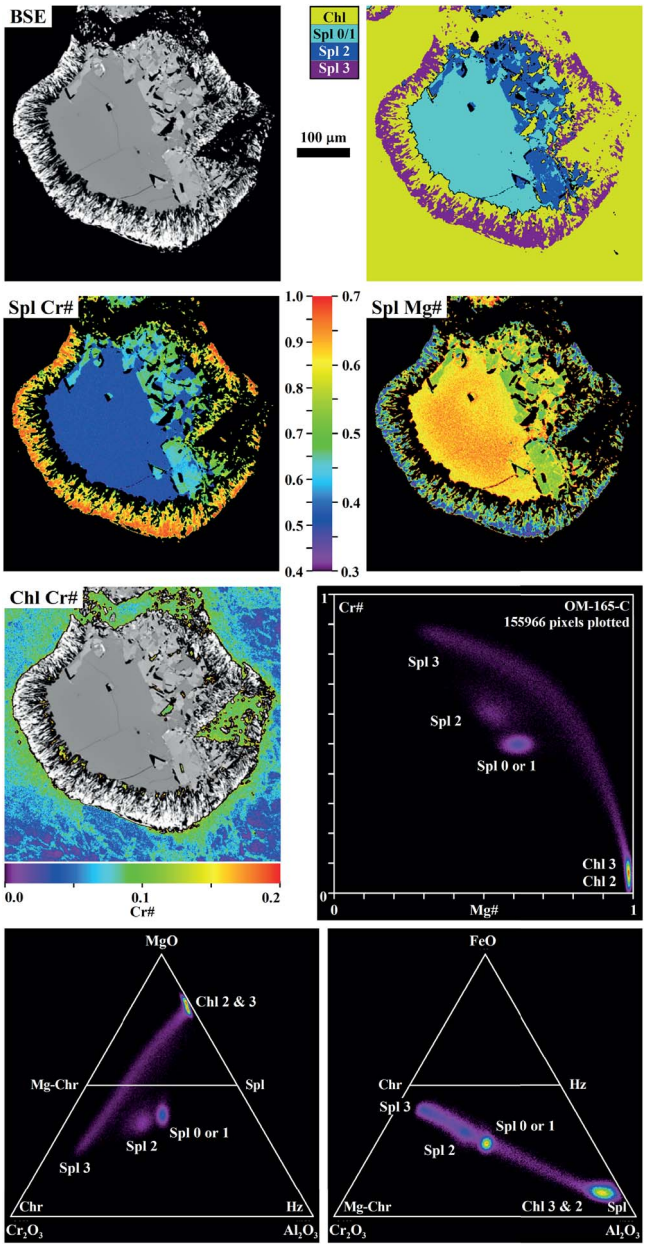

Fig. 16. Textural–chemical details of largely transformed spinel and chlorite of sample OM-165-C. All images and plots as in Fig. 14.

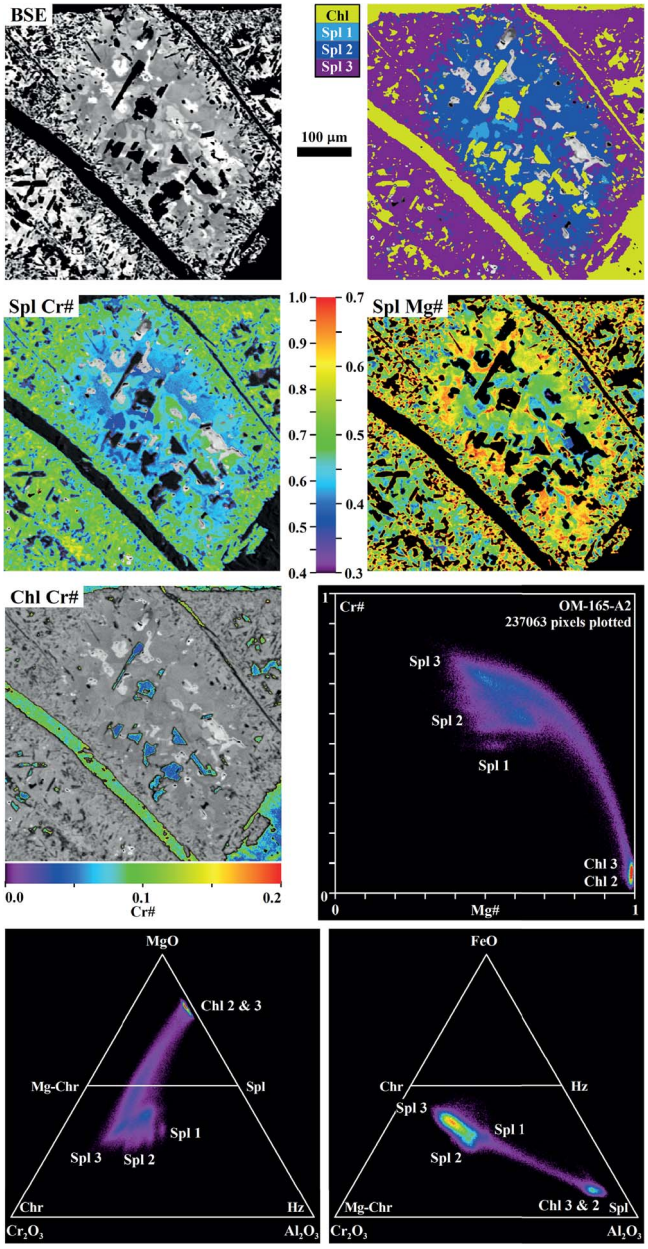

Fig. 17. Textural–chemical details of completely transformed spinel and chlorite of sample OM-165-A1. All images and plots as in Fig. 14.

potentially infinite extracted compositions of variable mixtures do not represent effective bulk compositions at reaction sites, for only products of reaction are measured in the maps. However, some examples of bulk-rock composition extracted from areas of the XR maps of Figs 15 and 16 (samples OM-165A2 and OM-165C, respectively) are given in Table 3 and illustrated in Fig. 19. As expected, these (and all) compositions of spinel+chlorite mixtures lie within the theoretical Spl–Chl (10-4-6 Chl–9-6-5 Chl) area of Fig. 19 and away from the olivine-spinel tie-line. These local compositions hence represent transformed spinel+olivine mixtures. The lack of knowledge of the multicomponent vectors associated with metasomatism precludes calculating the original compositions. However, assuming SiO_2 addition only, the suspected original compositions were estimated by subtracting SiO_2 from Spl2 + Chl2 mixtures up to reaching pure spinel-olivine mixtures (Table 3, Fig. 19).

Reaction progress

The sequence of spinel and chlorite compositions modelled in section 'General Petrologic Model' is confirmed by the study case of the Calzadilla metaophiolite. Similar mass-balance and thermodynamic calculations applied to this case study mirror those of the general model.

Mass-balance calculations are not offered for concision, but the relations between mineral compositions and extracted calculated local bulk compositions illustrated in Fig. 20, which includes Spl–Chl tie-lines representing model $K_{Ds}^{Spl2b\text{-}Chl2b}$ (Figs 6–8), satisfactorily explain qualitatively the process. Spl1, with subtle change in Mg# relative to Spl0 and constant Cr#, formed due to Fe–Mg exchange with olivine under anhydrous conditions. The lack of olivine relics prevents calculating the temperature conditions of this process. The formation of Spl2 + Chl2, with composition of spinel only slightly deviated from Spl0/Spl1, is the first step

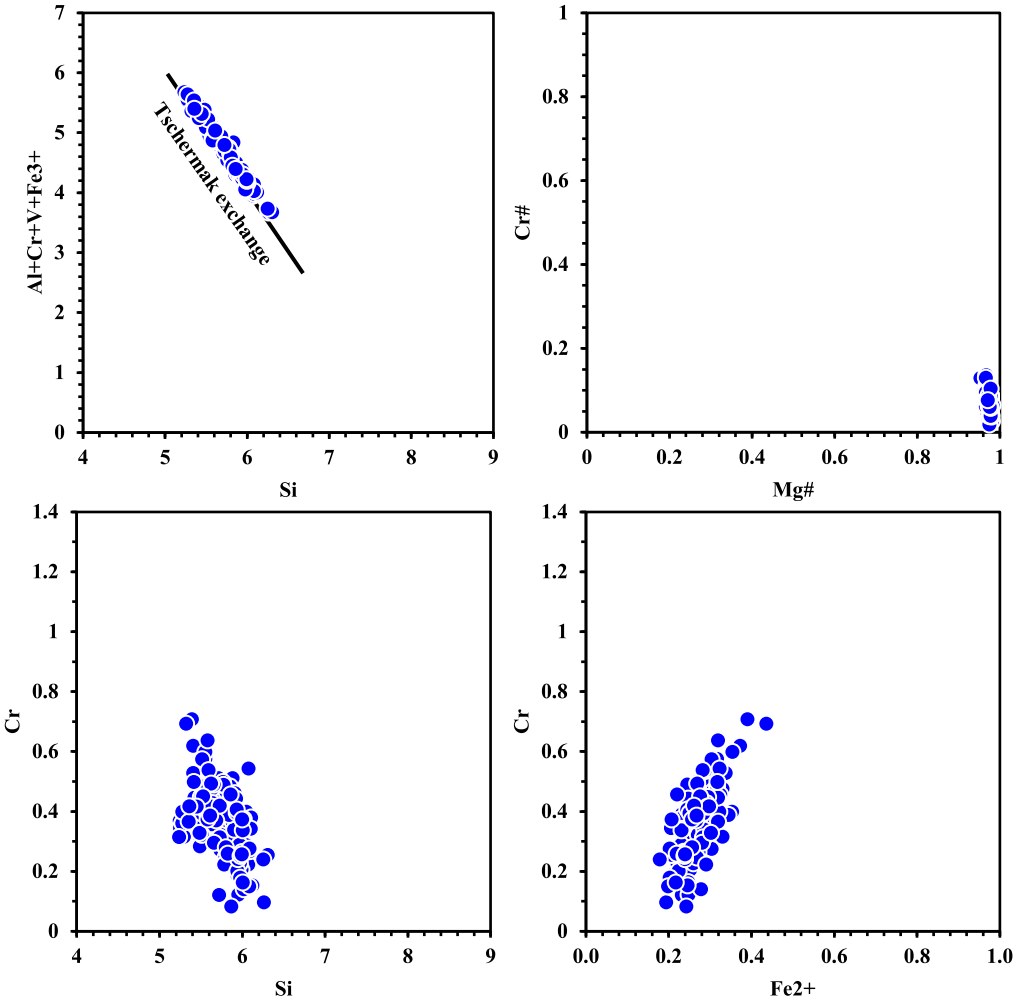

Fig. 18. Bivariate plots describing the composition of chlorite (147 point analyses). Note the similarity of the Cr# vs Mg# plot with the same plot in Figs 14–17.

of reaction progress characterized by olivine consumption (cf. eqs. 18 and 19). Clustered mild compositional deviation of Spl2 from Spl0/1 suggests that olivine was exhausted rapidly at near-constant temperature. The formation of relatively large idioblastic blocky Spl2 at this stage indicates a prograde metamorphic process or (near) isothermal-isobaric peak metamorphic conditions, in agreement with tectonic burial and regional metamorphism of the crustal and mantle sections of the metaophiolite (Novo-Fernández *et al.*, 2024). On the other hand, the formation of fine-grained Spl3 + Chl3 intergrowths after Spl0, Spl1 and Spl2, the increased amount of chlorite relative to step 2, and the strong Fe–Cr deviations from this type of spinel, suggest a dissolution-precipitation reaction in an olivine-absent scenario driven by infiltration of Si-richer fluid (cf. eq. 9, Figs 4 and 8). Buffering of this fluid by the solid assemblage spinel-chlorite is warranted given the lack of any other phase added during the evolving effective bulk composition at local reaction sites. Such buffering capability was accompanied by extreme changes in spinel composition upon decreasing its volume and the Spl3/Chl3 ratio of local bulk composition. Since this process simply marks the exhaustion of olivine, it is not necessarily related to cooling (cf. Merinero *et al.*, 2014). We interpret delicate reaction progress features involving both Spl2 + Chl2 and Spl3 + Chl3 (Fig. 12) as the result of continuity in the Spl + Chl-forming process during continued fluid infiltration at constant P–T or heating.

P–T conditions of transformation

The P–T conditions of the transformations cannot be calculated precisely, given the aforementioned lack of thermodynamic data for Cr-bearing chlorite solid solution. However, as explained above in section 'Thermodynamic model', we have performed pseudosection calculations to offer a first-order estimation using a diversity of bulk compositions extracted from the XR maps (Table 3, Fig. 19). All these calculations are benefited by relatively low-Cr in chlorite, particularly Chl2 (Fig. 20).

The results for sample OM-165A2 are shown in Fig. 21. This sample was selected to warrant a closer approximation of the calculated model with the natural case study because of its less-extreme composition of spinel Spl3 (Fig. 20). It can be appreciated that the stability of Spl2 + Chl2 and Spl3 + Chl3 are similar in P–T space (Fig. 21a and b, respectively) implying that Spl3 + Chl3 is not a retrograde assemblage of Spl2 + Chl2. Contrary to this result, if the P–T path of the Calzadilla metachromitites was to be inferred from a single P–T pseudosection using a single fixed bulk-composition, Spl3 + Chl3 in the metachromitite would be considered retrograde, as deduced by the $Cr\#^{Spl}$ isopleths. But this conclusion would be just apparent because the procedure of fixing a bulk composition does not obviously consider metasomatism during reaction progress.

It can be appreciated that $Cr\#^{Spl}$ and the volume of spinel are strictly negatively correlated in the P–T diagrams of Fig. 21,

Table 3: Examples of bulk compositions (molar units) extracted from XR maps of Figs 15 and 16 and calculated original spinel+olivine mixtures after subtracting SiO_2 from Spl2 + Chl2 mixtures

Sample	OM-165A2			OM-165C		
Type	Spl2 + Chl2	Spl3 + Chl3	Spl2 + Chl2–SiO_2	Spl2 + Chl2	Spl3 + Chl3	Spl2 + Chl2–SiO_2
SiO_2	16.9	23.4	11.7	9.2	24.1	6.2
Al_2O_3	16.5	12.5	17.6	18.6	11.0	19.2
Cr_2O_3	14.1	10.5	14.9	20.8	11.1	21.5
FeO	11.3	8.7	12.0	17.0	9.2	17.6
MgO	41.3	44.9	43.9	34.3	44.6	35.5
Sum	100.0	100.0	100.0	100.0	100.0	100.0

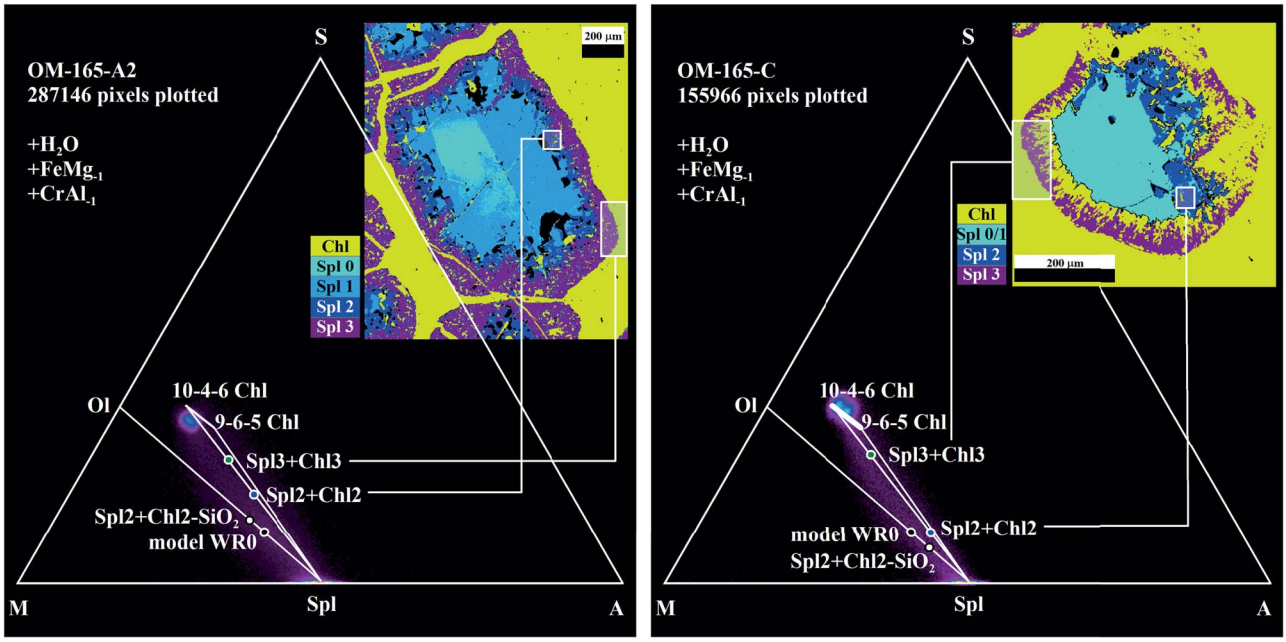

Fig. 19. MAS plots of bulk compositions extracted from the XR maps of Figs 15 and 16 (samples OM-165A2 and OM-165C, respectively). The areas are indicated in the insets, representing mixtures of Spl2 + Chl2 and Spl3 + Chl3 as indicated in the phase maps (Chl types not shown). These bulk compositions are not to be considered effective bulk compositions at reaction sites. Model WR0 and the restored compositions of the samples to Spl + Ol mixtures, calculated subtracting SiO_2 from Spl2 + Chl2 and used as starting point of thermodynamic calculations, are plotted for comparison.

implying a major effect of spinel volume reduction on $Cr\#^{Spl}$. As noted above in the section 'General petrologic model', this result is the consequence of the fractionation of chromium only by spinel in the thermodynamic calculations. This drawback also explains the constant $Cr\#^{Spl}$ and $Vol\%^{Spl}$ at varied P–T in the 5-variant Spl + Chl + Fluid field of Fig. 21. However, the above conclusion is echoed in the natural case provided that other coexisting phases, including chlorite, do not strongly fractionate this element, as shown in Fig. 20. In short, calculating the distribution of Cr# isopleths in P–T space for a fixed bulk composition and comparing it with the composition of natural samples is not a wise procedure for ascertaining transformation processes in metachromitites in a chemically changing medium nor, of course, for ascertaining the temperature of transformation.

The effects of changing the chemical composition of the system are approximated in the T-X pseudosection of Fig. 21c). The emphasis of this plot is that increasing Cr# in spinel is a function of spinel volume reduction in the Spl + Chl + Fluid field. The corresponding P–T diagrams for Spl2 + Chl2 and Spl3 + Chl3 and this T-X plot simply indicate that increased Cr in spinel is not necessarily a retrograde feature relative to previous spinel+chlorite steps of development, as predicted in the general petrologic model (Fig. 9). For the studied case, we conclude that all transformation processes took place at (or near) the isobaric-isothermal conditions of peak metamorphism in the Calzadilla metaophiolite (525–575°C, 0.4–0.5 GPa; Novo-Fernández *et al.*, 2024).

Implications for the Calzadilla metaophiolite

The processes described above for the Calzadilla metachromitite are consistent with a (near) synchronous textural-mineral composition development, implying near-constant pressure and temperature. This is at odds with previous interpretations of the studied ophiolitic chromitite that emphasize sequential development upon continuous hydration and cooling (Merinero *et al.*, 2014). However, such scenario is only possible if fluid infiltration was fully coupled with cooling. That is, a slow cooling rate after regional collision-related metamorphism needs a continuous low fluid infiltration rate to prevent full hydration (Spl2 + Chl2 + Fluid) of the original olivine+spinel assemblage. In our view, two fully unconnected processes

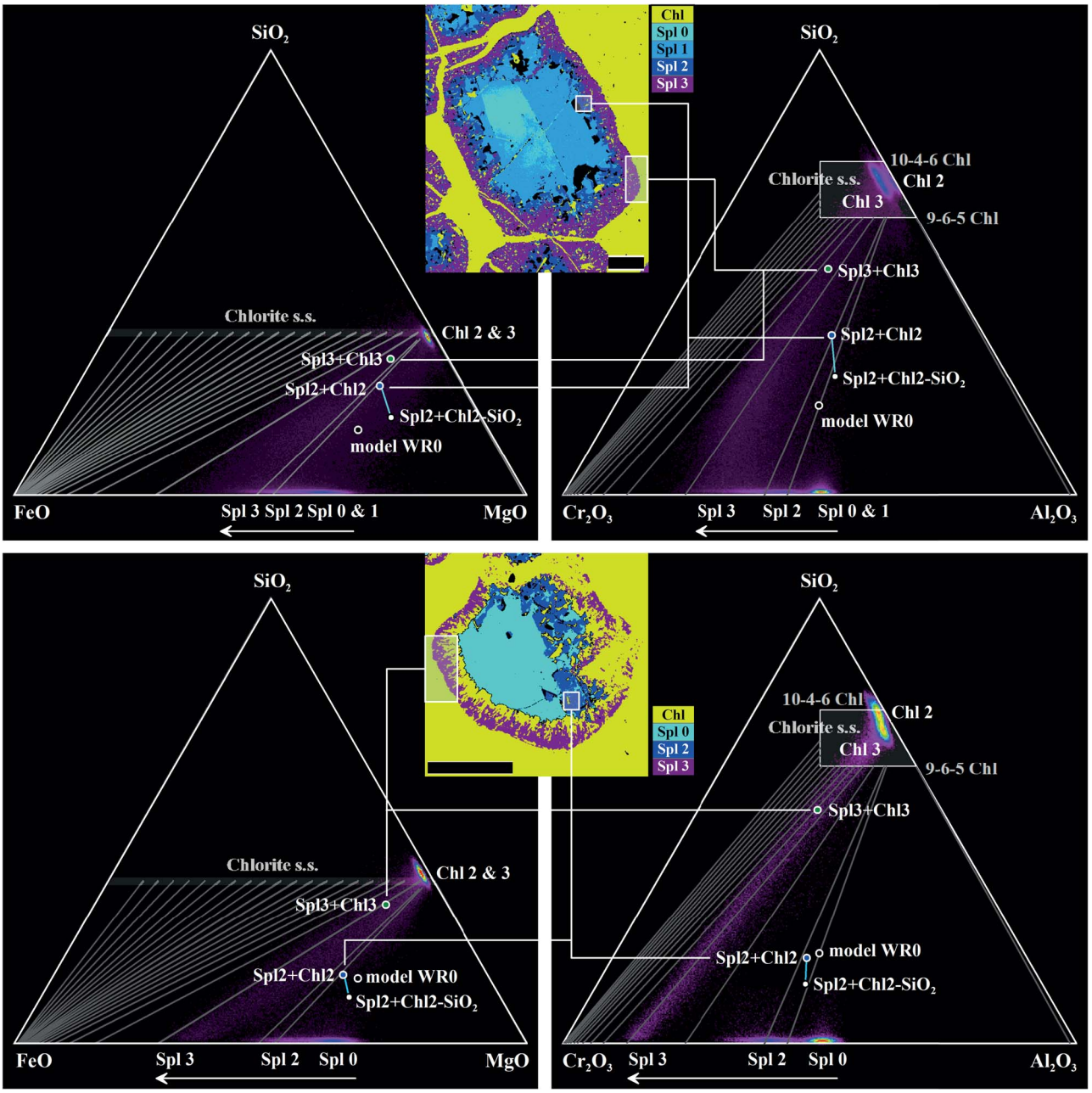

Fig. 20. FeO–MgO–SiO_2 and Cr_2O_3–Al_2O_3–SiO_2 diagrams showing the textural-composition relations of spinel and chlorite from two chromitite samples from the Calzadilla metaophiolite shown in Figs 15, 16 and 19. The tie-lines are for K_{Ds} for model WR2b depicted in Figs 6–8.·The compositions are extracted from the XR maps of Figs 15 and 16 (samples OM-165A2 and OM-165C, respectively). The areas are indicated in the insets, representing mixtures areas of Spl2 + Chl2 and Spl3 + Chl3 as indicated in the phase maps (Chl types not shown). These bulk compositions are not to be considered effective bulk compositions at reaction sites. Model WR0 and the restored compositions of the samples Spl + Ol mixtures, calculated subtracting SiO_2 from Spl2 + Chl2 and used as starting point of thermodynamic calculations, are plotted for comparison.

such as cooling, mainly controlled by heat diffusion, and fluid infiltration, mainly controlled by the mechanical failure and permeability of rocks, cannot progress under such singularly coupled rates. Thus, the expected rapid hydration and associated complete exhaustion of olivine early in the slow cooling history of the metaophiolite would have triggered formation of Spl2 + Chl2 and high Cr Spl3 + Chl3 at similar temperature.

The inferred near-isobaric-isothermal P–T conditions of near-synchronous transformation of the Calzadilla ophiolitic chromitite samples are fully in accordance with independent estimations of the metamorphic processes undergone by associated metaperidotites and amphibolites of the mantle and crustal sections, respectively, of the ophiolite. This clearly points to transformation during the Cadomian prograde evolution of the unit. Thus, our inferences are consistent with near-full hydration of the mantle and crustal sections of the ophiolite during prograde metamorphism. Relics of mantle olivine, pyroxenes and spinel in the metaperidotites and of magmatic pyroxene and plagioclase in the metabasic rocks are extremely rare in the Calzadilla ophiolite (Fernández Carrasco *et al.*, 1980; Arriola *et al.*, 1984; Aguayo Fernández, 1985; Novo-Fernández *et al.*, 2024). Though partial hydration during cooling at low pressure in the forearc setting of formation of the ophiolite is not excluded, the rarity of

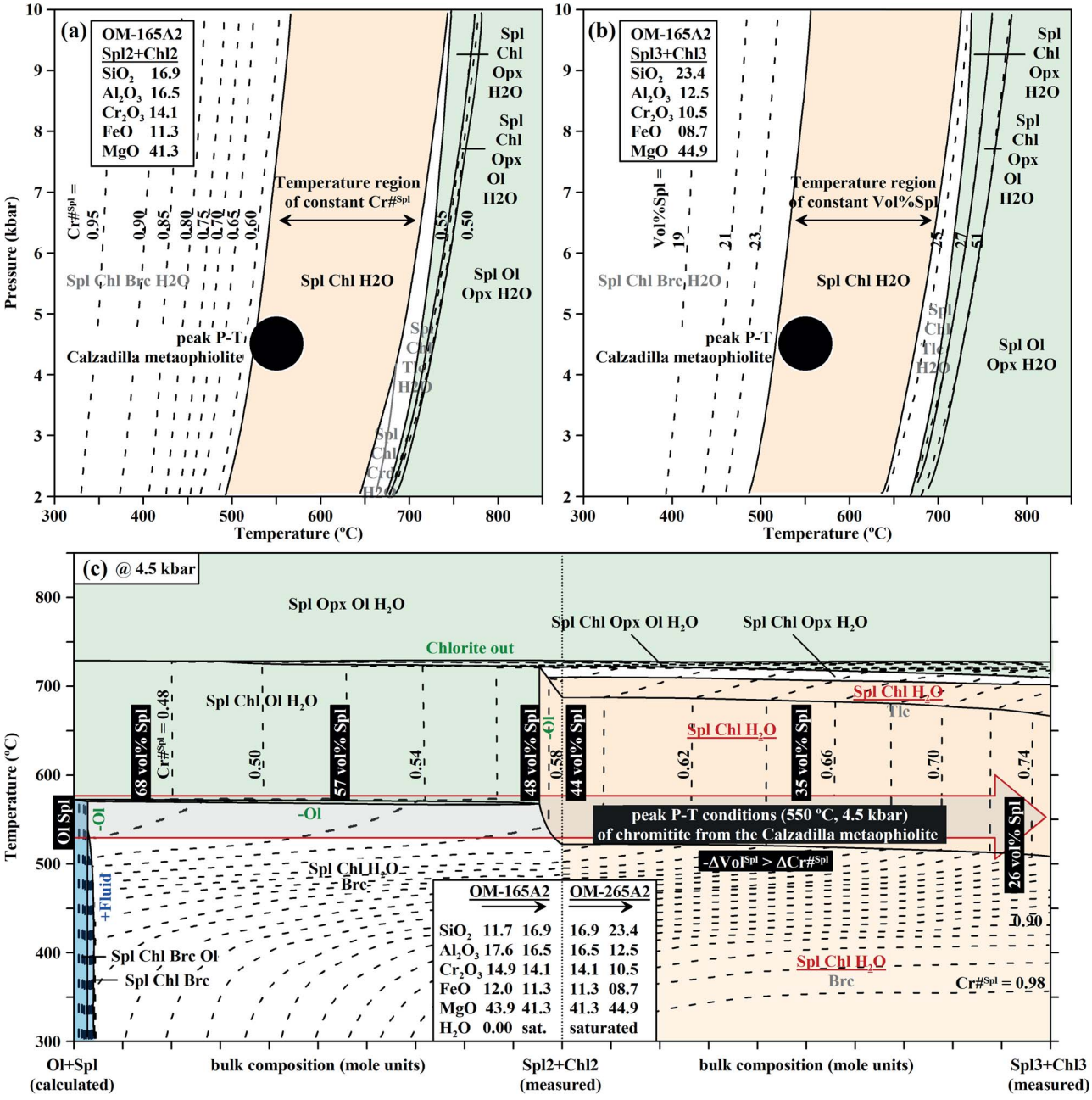

Fig. 21. A and B: P–T pseudosections in the FMACrSH system for bulk compositions Spl2 + Chl2 and Spl3 + Chl3, respectively, extracted from chromitite sample OM-165A2 (Table 3). Note that the isopleths of Cr#Spl (left) and vol%Spl (right) show constant values in the temperature region of the Spl + Chl stability field. Also indicated are the peak conditions of the Calzadilla metaophiolite (Novo-Fernández *et al.*, 2024). C: T-X pseudosection (at 0.45 GPa) starting with an anhydrous bulk composition calculated subtracting SiO_2 from Spl2 + Chl2 to reach a pre-transformation Ol-Spl mixture (Table 3, Fig. 19). See text for further explanation.

relics in metaperidotites and metabasites argues in favor of near-full hydration during prograde metamorphism in a context of crustal thickening and dehydration of nearby metasedimentary units (Serie Negra), rather than during retrograde cooling. Zoned grains of amphibole in the metabasites denote core-to-rim growth during increasing temperature and pressure, hence proving that near-full hydration was accomplished during their prograde path. A similar scenario is envisaged in the metaperidotites. Hence it is extremely improbable that an insignificantly small portion of the unit, the chromitites of the mantle section, eluded hydration during prograde metamorphism.

CONCLUSIONS

The general petrologic model presented here for the metamorphic/metasomatic transformation of chromitite in the FMACrSH system yields the same trend in mineral assemblage and mineral composition during either isothermal-isobaric conditions, heating or cooling. That the progress of reaction yields the same product under variable P–T conditions and paths is the result of metasomatic changes of the bulk composition of chromitite towards the Spl + Chl assemblage, an extremely stable assemblage in P–T space below ca. 800°C (i.e. below the maximum stability of chlorite in this chemical system). Provided the availability of fluid, the main driving forces for the

chemical trend of spinel are, sequentially but eventually almost synchronously provided full hydration, a) the consumption of olivine, which is reached early in the reaction progress due to the high Spl/Ol ratios in the rocks and the higher stoichiometric coefficient of olivine relative to spinel (both normalized to 4 oxygens) in eq. 6, and b) the progressive metasomatic change of local bulk composition towards chlorite at olivine-lacking 5-variant Spl + Chl + Fluid reaction sites upon fluid infiltration from external sources, likely the surrounding serpentinites. The first model step a) produces restricted composition in spinel that is not largely deviated from the original metastable mantle spinel and b) relatively constant Spl/Chl ratios, as a function of original Spl/Ol ratios. The second step triggers a) the progressive decrease and increase in the volume of spinel and chlorite, respectively, and b) a correlated increase in Fe–Cr-spinel compositions that continuously deviates from mantle spinel composition, as a function of continued infiltration of external fluid in the 5-variant Spl + Chl + Fluid assemblage. A main implication of this model is that an increase in Cr# and decreases in Mg# of transformed spinel does not necessarily mean retrogression relative to previous steps in the textural-mineral development of transformed chromitite. In turn, extreme compositions are more the result of decreasing spinel volume at reaction sites, even if temperature increases relative to previous steps.

The predictions of the petrologic model are mirrored in the natural world, implying that metasomatism triggered by reaction with an external fluid is general in metachromitites and that their textural-mineral development is not necessarily related to cooling, as commonly assumed. In the case-study revisited here of the Calzadilla metaophiolite we conclude that the whole textural-mineral development described here as Spl2 + Chl2 and Spl3 + Chl3 is prograde or near-isothermal-isobaric at the peak conditions of the metaophiolite (ca. 550°C, ca. 0.45 GPa). Like this one, other previously described case-studies of retrograde textural-mineral development in regionally metamorphosed chromitite should be perhaps reconsidered in light of the general petrologic model offered here. However, future work for progressing in the geologic/geodynamic environment of chromitite (and ultramafic rocks) transformation process requires development of experimental studies at subsolidus conditions in Cr-bearing systems to validate the proposed model's predictions and, importantly, to gather critical compositional data for developing thermodynamic properties of Cr-bearing phases, in particular chlorite. These properties, if implemented in current thermodynamic databases, would allow constructing more accurate phase diagrams and evaluating element partitioning among coexisting phases upon cooling vs. heating and under closed vs open system conditions.

SUPPLEMENTARY DATA

Supplementary data are available at *Journal of Petrology* online.

ACKNOWLEDGEMENTS

We thank the editors Georg Zellmer and Reto Gieré for editorial handling, reviewer Pengfei Zhang and two anonymous reviewers, and Fernando Gervilla, for comments that improved the clarity of the manuscript, and Xavier Llovet for his careful EPMA work at CCiT, Barcelona University.

DATA AVAILABILITY

The data underlying this article are available in the article, its online Supplementary Material Table 1 and in the Earth-Chem Library repository (Garcia-Casco *et al.*, 2024; https://doi.org/10.60520/IEDA/113507).

FUNDING

This work was supported by Spanish Ministry of Science, Innovation and Universities (projects PID2019-105625RB-C21, PID2020-112489GB-C21 and PID2020-114872GB-I00 to J.A.P., R.A. and J.F.M., respectively), 'Juan de la Cierva' postdoctoral contracts JDC2022-048971-I and JDC2022-049113-I to N.P.-S. and I.N.-F., respectively, and pre-doctoral FPI contracts PRE2021-098916 and PRE 2020-092140 to G.I. and D.D.-C., respectively. Funding for open access charge: Universidad de Granada/CBUA.

REFERENCES

Aguayo Fernández, J. M. (1985) *Rocas ultramáficas en el sector de Calzadilla de los Barros (Badajoz)*Universidad del País Vasco, Tesis de Licenciatura, p.115.

Angiboust, S., Yamato, P., Hertgen, S., Hyppolito, T., Bebout, G. E. & Morales, L. (2017). Fluid pathways and high-P metasomatism in a subducted continental slice (Mt. Emilius klippe, W. Alps). *Journal of Metamorphic Geology* **35**, 471–492. https://doi.org/10.1111/jmg.12241.

Angiboust, S., Glodny, J., Cambeses, A., Raimondo, T., Monié, P., Popov, M. & Garcia-Casco, A. (2021). Drainage of subduction interface fluids into the forearc mantle evidenced by a pristine jadeitite network (Polar Urals). *Journal of Metamorphic Geology* **39**, 473–500. https://doi.org/10.1111/jmg.12570.

Arai, S. & Matsukage, K. (1998). Petrology of a chromitite micropod from Hess Deep, equatorial Pacific: a comparison between abyssal and alpine-type podiform chromitites. *Lithos* **43**, 1–14. https://doi.org/10.1016/S0024-4937(98)00003-6.

Arai, S. & Miura, M. (2016). Formation and modification of chromitites in the mantle. *Lithos* **264**, 277–295. https://doi.org/10.1016/j.lithos.2016.08.039.

Arai, S., Shimizu, Y., Ismail, S. A. & Ahmed, A. H. (2006). Low-T formation of high-Cr spinel with apparently primary chemical characteristics within podiform chromitite from Rayat, northeastern Iraq. *Mineralogical Magazine* **70**, 499–508. https://doi.org/10.1180/0026461067050353.

Arenas, R., Fernández-Suárez, J., Montero, P., Díez Fernández, R., Andonaegui, P., Sánchez Martínez, S., Albert, R., Fuenlabrada, J. M., Matas, J., Martín Parra, L. M., Rubio Pascual, F. J., Jiménez-Díaz, A. & Pereira, M. F. (2018). The Calzadilla Ophiolite (SW Iberia) and the Ediacaran fore-arc evolution of the African margin of Gondwana. *Gondwana Research* **58**, 71–86. https://doi.org/10.1016/j.gr.2018.01.015.

Arenas, R., Vérard, C., Albert, R., Rojo-Pérez, E., Sánchez Martínez, S., Novo-Fernández, I., Moreno-Martín, D., Gerdes, A., Garcia–Casco, A. & Díez Fernández, R. (2024). Cadomia origins: paired Ediacaran ophiolites from the Iberian Massif, the opening and closure record of peri-Gondwanan basins. *Geological Society, London, Special Publications* **542**, 507–526. https://doi.org/10.1144/SP542-2022-328.

Arriola, A., Cueto Pascual, L. A., Fernández Carrasco, J. & Garrote, A. (1984). Serpentinitas y mineralizaciones de cromo asociadas en el Proterozoico superior de Ossa Morena. *Cadernos do Laboratorio Xeoloxico de Laxe* **8**, 137–146.

Barra, F., Gervilla, F., Hernández, E., Reich, M., Padrón-Navarta, J. A. & González-Jiménez, J. M. (2014). Alteration patterns of chromian spinels from La Cabaña peridotite, south-central Chile. *Mineralogy and Petrology* **108**(6), 819–836. https://doi.org/10.1007/s00710-014-0335-5.

Blanco-Quintero, I. F., Rojas-Agramonte, Y., García-Casco, A., Kröner, A., Mertz, D. F., Lázaro, C., Blanco-Moreno, J. & Renne, P. R. (2011). Timing of subduction and exhumation in a subduction channel: evidence from slab melts from La Corea Mélange (eastern Cuba). *Lithos* **127**, 86–100. https://doi.org/10.1016/j.lithos.2011.08.009.

Borisova, A. Y., Ceuleneer, G., Kamenetsky, V. S., Arai, S., Béjina, F., Abily, B., Bindeman, I. N., Polvé, M., De Parseval, P., Aigouy, T. & Pokrovski, G. S. (2012). A new view on the petrogenesis of the Oman Ophiolite chromitites from microanalyses of chromite-hosted inclusions. *Journal of Petrology* **53**, 2411–2440. https://doi.org/10.1093/petrology/egs054.

Brady, J. B. & Stout, J. H. (1980). Normalizations of thermodynamic properties and some implications for graphical and analytical problems in petrology. *American Journal of Science* **280**, 173–189. https://doi.org/10.2475/ajs.280.2.173.

Colás, V., Padrón-Navarta, J. A., González-Jiménez, J. M., Griffin, W. L., Fanlo, I., O'Reilly, S. Y., Gervilla, F., Proenza, J. A., Pearson, N. J. & Escayola, M. P. (2016). Compositional effects on the solubility of minor and trace elements in oxide spinel minerals: insights from crystal–crystal partition coefficients in chromite exsolution. *American Mineralogist* **101**, 1360–1372. https://doi.org/10.2138/am-2016-5611.

Colás, V., Padrón-Navarta, J. A., González-Jiménez, J. M., Fanlo, I., López Sánchez-Vizcaíno, V., Gervilla, F. & Castroviejo, R. (2017). The role of silica in the hydrous metamorphism of chromite. *Ore Geology Reviews* **90**, 274–286. https://doi.org/10.1016/j.oregeorev.2017.02.025.

Colás, V., González-Jiménez, J. M., Camprubí, A., Proenza, J. A., Griffin, W. L., Fanlo, I., O'Reilly, S. Y., Gervilla, F. & González-Partida, E. (2019). A reappraisal of the metamorphic history of the Tehuitzingo chromitite, Puebla state, Mexico. *International Geology Review* **61**, 1706–1727. https://doi.org/10.1080/00206814.2018.1542633.

Colás, V., Subías, I., González-Jiménez, J. M., Proenza, J. A., Fanlo, I., Camprubí, A., Griffin, W. L., Gervilla, F., O'Reilly, S. Y. & Escayola, M. P. (2020). Metamorphic fingerprints of Fe-rich chromitites from the Eastern Pampean Ranges, Argentina. *Boletín de la Sociedad Geológica Mexicana* **72**, A080420.

Díez Fernández, R., Jiménez-Díaz, A., Arenas, R., Pereira, M. F. & Fernández-Suárez, J. (2019). Ediacaran obduction of a fore-arc ophiolite in SW Iberia: a turning point in the evolving geodynamic setting of Peri-Gondwana. *Tectonics* **38**, 95–119. https://doi.org/10.1029/2018TC005224.

Engi, M. (1983). Equilibria involving Al–Cr spinel: Mg–Fe exchange with olivine. Experiments, thermodynamic analysis, and consequences for geothermometry. *American Journal of Science* **283**, 29–71.

Epstein, G. S., Bebout, G. E. & Angiboust, S. (2021). Fluid and mass transfer along transient subduction interfaces in a deep paleo-accretionary wedge (Western Alps). *Chemical Geology* **559**, 119920. https://doi.org/10.1016/j.chemgeo.2020.119920.

Epstein, G. S., Condit, C. B., Stoner, R. K., Holt, A. F. & Guevara, V. E. (2024). Evolving subduction zone thermal structure drives extensive forearc mantle wedge hydration. *AGU Advances* **5**, e2023AV001121. https://doi.org/10.1029/2023AV001121.

Eslami, A., Malvoisin, B. & Brunet, F. (2023). Hydrothermal alteration of chromitite–dunite pairs from the Sabzevar ophiolite (NE Iran): chemical and nano-textural evolution of Cr-spinel. *Lithos* **442-443**, 107093. https://doi.org/10.1016/j.lithos.2023.107093.

Fabriès, J. (1979). Spinel-olivine geothermometry in peridotites from ultramafic complexes. *Contributions to Mineralogy and Petrology* **69**, 329–336. https://doi.org/10.1007/BF00372258.

Fernández Carrasco, J., Portero García, J.M., Garrote, A., Arriola, A., Eguiluz, L., Sánchez Carretero, R., Quesada, C. & Cueto, L.A. (1980). Mapa Geológico Nacional E. 1:50000 (Serie MAGNA), hoja n° 876 (Fuente de Cantos). Instituto Geológico y Minero de España (IGME), Madrid.

Festa, A., Dilek, Y., Pini, G. A., Codegone, G. & Ogata, K. (2012). Mechanisms and processes of stratal disruption and mixing in the development of mélanges and broken formations: redefining and classifying mélanges. *Tectonophysics* **568-569**, 7–24. https://doi.org/10.1016/j.tecto.2012.05.021.

Fisher, G. W. (1993). An improved method for algebraic analysis of metamorphic mineral assemblages. *American Mineralogist* **78**, 1257–1261.

García-Casco, A. (2007). Magmatic paragonite in trondhjemites from the Sierra del Convento mélange, Cuba. *American Mineralogist* **92**, 1232–1237. https://doi.org/10.2138/am.2007.2598.

García-Casco, A., Torres-Roldán, R. L., Millán, G., Monié, P. & Schneider, J. (2002). Oscillatory zoning in eclogitic garnet and amphibole, Northern Serpentinite Melange, Cuba: a record of tectonic instability during subduction? *Journal of Metamorphic Geology* **20**, 581–598. https://doi.org/10.1046/j.1525-1314.2002.00390.x.

García-Casco, A., Torres-Roldán, R. L., Iturralde-Vinent, M., Millán, G., Núñez Cambra, K., Lázaro Calisalvo, C. & Rodríguez Vega, A. (2006). High-pressure metamorphism of ophiolites in Cuba. *Geologica Acta* **4**, 63–88.

Garcia-Casco, A., Lázaro, C., Rojas-Agramonte, Y., Kröner, A., Torres-Roldán, R. L., Núñez, K., Neubauer, F., Millán, G. & Blanco-Quintero, I. F. (2008). Partial melting and counterclockwise P T path of subducted oceanic crust (sierra del Convento Melange, Cuba). *Journal of Petrology* **49**, 129–161. https://doi.org/10.1093/petrology/egm074.

Garcia-Casco, A., Restrepo, J. J., Correa-Martínez, A. M., Blanco-Quintero, I. F., Proenza, J. A., Weber, M. & Butjosa, L. (2020) The petrologic nature of the "Medellín Dunite" revisited: an algebraic approach and proposal of a new definition of the geological body. In: Gómez J. & Pinilla-Pachon A. O. (eds) *The Geology of Colombia, Volume 2 Mesozoic*. Publicaciones Geológicas Especiales: Servicio Geológico Colombiano, pp.45–75.

Garcia-Casco, A., Pujol-Solà, N., Novo-Fernández, I., Arenas, R., Rojo-Pérez, E., Cambeses, A., Molina, J. F., Sánchez Martínez, S., Domínguez-Carretero, D., Iglesias, G. & Proenza, J. A. (2024). Quantitative major elements EMPA analyses of spinel and chlorite from metamorphic chromitites of the Calzadilla Ophiolite (SW Iberian Massif). Version 1.0. Interdisciplinary Earth Data Alliance (IEDA). https://doi.org/10.60520/IEDA/113507.

Gervilla, F., Padrón-Navarta, J. A., Kerestedjian, T., Sergeeva, I., González-Jiménez, J. M. & Fanlo, I. (2012). Formation of ferrian chromite in podiform chromitites from the Golyamo Kamenyane serpentinite, Eastern Rhodopes, SE Bulgaria: a two-stage process. *Contributions to Mineralogy and Petrology* **164**, 643–657. https://doi.org/10.1007/s00410-012-0763-3.

Gervilla, F., Asta, M. P., Fanlo, I., Grolimund, D., Ferreira-Sánchez, D., Samson, V. A., Hunziker, D., Colas, V., González-Jiménez, J. M., Kerestedjian, T. N. & Sergeeva, I. (2019). Diffusion pathways of Fe^{2+} and Fe^{3+} during the formation of ferrian chromite: a μXANES study. *Contributions to Mineralogy and Petrology* **174**, 65. https://doi.org/10.1007/s00410-019-1605-3.

González-Jiménez, J. M., Kerestedjian, T., Proenza, J. A. & Gervilla, F. (2009). Metamorphism on chromite ores from the Dobromirtsi Ultramafic Massif, Rhodope Mountains (SE Bulgaria). *Geologica Acta* **7**, 413–429.

González-Jiménez, J. M., Griffin, W. L., Proenza, J. A., Gervilla, F., O'Reilly, S. Y., Akbulut, M., Pearson, N. J. & Arai, S. (2014). Chromitites in ophiolites: how, where, when, why? Part II. The crystallization of chromitites. *Lithos* **189**, 140–158. https://doi.org/10.1016/j.lithos.2013.09.008.

González-Jiménez, J. M., Locmelis, M., Belousova, E., Griffin, W. L., Gervilla, F., Kerestedjian, T. N., O'Reilly, S. Y., Pearson, N. J. & Sergeeva, I. (2015a). Genesis and tectonic implications of podiform chromitites in the metamorphosed ultramafic massif of Dobromirtsi (Bulgaria). *Gondwana Research* **27**, 555–574. https://doi.org/10.1016/j.gr.2013.09.020.

González-Jiménez, J. M., Reich, M., Camprubí, A., Gervilla, F., Griffin, W. L., Colás, V., O'Reilly, S. Y., Proenza, J. A., Pearson, N. J. & Centeno-García, E. (2015b). Thermal metamorphism of mantle chromites and the stability of noble-metal nanoparticles. *Contributions to Mineralogy and Petrology* **170**, 15. https://doi.org/10.1007/s00410-015-1169-9.

González-Jiménez, J. M., Proenza, J. A., Martini, M., Camprubí, A., Griffin, W. L., O'Reilly, S. Y. & Pearson, N. J. (2017a). Deposits associated with ultramafic–mafic complexes in Mexico: the Loma Baya case. *Ore Geology Reviews* **81**, 1053–1065. https://doi.org/10.1016/j.oregeorev.2015.05.014.

González-Jiménez, J. M., Marchesi, C., Griffin, W. L., Gervilla, F., Belousova, E. A., Garrido, C. J., Romero, R., Talavera, C., Leisen, M., O'Reilly, S. Y., Barra, F. & Martin, L. (2017b). Zircon recycling and crystallization during formation of chromite- and Ni-arsenide ores in the subcontinental lithospheric mantle (Serranía de Ronda, Spain). *Ore Geology Reviews* **90**, 193–209. https://doi.org/10.1016/j.oregeorev.2017.02.012.

Hernández-González, J. S., Butjosa, L., Pujol-Solà, N., Aiglsperger, T., Weber, M., Escayola, M., Ramírez-Cárdenas, C., Blanco-Quintero, I. F., González-Jiménez, J. M. & Proenza, J. A. (2020). Petrology and geochemistry of high-Al chromitites from the Medellin Metaharzburgitic Unit (MMU), Colombia. *Boletín de la Sociedad Geológica Mexicana* **72**, A120620. https://doi.org/10.18268/BSGM2020v72n3a120620.

Holland, T. J. B. & Powell, R. (1998). An internally consistent thermodynamic data set for phases of petrological interest. *Journal of Metamorphic Geology* **16**, 309–343. https://doi.org/10.1111/j.1525-1314.1998.00140.x.

Holland, T. J. B. & Powell, R. (2011). An improved and extended internally consistent thermodynamic dataset for phases of petrological interest, involving a new equation of state for solids. *Journal of Metamorphic Geology* **29**, 333–383. https://doi.org/10.1111/j.1525-1314.2010.00923.x.

Holland, T. J. B., Green, E. C. R. & Powell, R. (2018). Melting of peridotites through to granites: a simple thermodynamic model in the system KNCFMASHTOCr. *Journal of Petrology* **59**, 881–900. https://doi.org/10.1093/petrology/egy048.

Hyppolito, T., Angiboust, S., Juliani, C., Glodny, J., Garcia-Casco, A., Calderon, M. & Chopin, C. (2016). Eclogite-, amphibolite- and blueschist-facies rocks from Diego de Almagro Island (Patagonia): episodic accretion and cretaceous thermal evolution of the Chilean subduction interface. *Lithos* **264**, 422–440. https://doi.org/10.1016/j.lithos.2016.09.001.

Jenkins, D. M. (1981). Experimental phase relations of hydrous peridotites modelled in the system H_2O–CaO–MgO–Al_2O_3–SiO_2. *Contributions to Mineralogy and Petrology* **77**, 166–176. https://doi.org/10.1007/BF00636520.

Jiménez-Díaz, A. (2008) *Análisis de los procesos de cizalla dúctil en el macizo peridotítico de Calzadilla de los Barros (Extremadura)*MSc Thesis,. Madrid, Spain: Universidad Complutense, p.51.

Jiménez-Díaz, A., Capote, R., Tejero, R., Lunar, R., Ortega, L., Monterrubio, S., Maldonado, C. & Rodríguez, D. (2009). La fábrica de las rocas miloníticas de la Zona de Cizalla de Los Ilanos (Calzadilla de los Barros, Badajoz). *Geogaceta* **46**, 27–30.

Kempf, E. D., Hermann, J. & Connolly, J. A. D. (2022). Serpentinite dehydration at low pressures. *Swiss Journal of Geosciences* **115**, 14. https://doi.org/10.1186/s00015-022-00415-y.

Klein, F., Humphris, S. E. & Bach, W. (2020). Brucite formation and dissolution in oceanic serpentinite. *Geochemical Perspectives Letters* **16**, 1–5. https://doi.org/10.7185/geochemlet.2035.

Lakey, S. & Hermann, J. (2022). An experimental study of chlorite stability in varied subduction zone lithologies with implications for fluid production, melting, and diapirism in chlorite-rich Mélange rocks. *Journal of Petrology* **63**, egac029. https://doi.org/10.1093/petrology/egac029.

Leblanc, M. & Nicolas, A. (1992). Ophiolitic chromititites. *International Geology Review* **34**, 653–686. https://doi.org/10.1080/00206819209465629.

Lehmann, J. (1983). Diffusion between olivine and spinel: application to geothermometry. *Earth and Planetary Science Letters* **64**, 123–138. https://doi.org/10.1016/0012-821X(83)90057-2.

Liu, J., Xia, Q.-K., Kuritani, T., Hanski, E. & Yu, H.-R. (2017). Mantle hydration and the role of water in the generation of large igneous provinces. *Nature Communications* **8**, 1824. https://doi.org/10.1038/s41467-017-01940-3.

Liu, X., Su, B.-X., Xiao, Y., Chen, C., Uysal, I., Jing, J.-J., Zhang, P.-F., Chu, Y., Lin, W. & Asamoah Sakyi, P. (2019). Initial subduction of Neo-Tethyan Ocean: geochemical records in chromite and mineral inclusions in the Pozantı-Karsantı ophiolite, southern Turkey. *Ore Geology Reviews* **110**, 102926. https://doi.org/10.1016/j.oregeorev.2019.05.012.

Malitch, K. N., Belousova, E. A., Griffin, W. L., Badanina, I. Y., Knauf, V. V., O'Reilly, S. Y. & Pearson, N. J. (2017). Laurite and zircon from the Finero chromitites (Italy): new insights into evolution of the subcontinental mantle. *Ore Geology Reviews* **90**, 210–225. https://doi.org/10.1016/j.oregeorev.2017.06.027.

Malvoisin, B. (2015). Mass transfer in the oceanic lithosphere: Serpentinization is not isochemical. *Earth and Planetary Science Letters* **430**, 75–85. https://doi.org/10.1016/j.epsl.2015.07.043.

Manning, C. E. & Frezzotti, M. L. (2020). Subduction-zone fluids. *Elements* **16**, 395–400. https://doi.org/10.2138/gselements.16.6.395.

Mark, H. F., Lizarralde, D. & Wiens, D. A. (2023). Constraints on bend-faulting and mantle hydration at the Marianas Trench from seismic anisotropy. *Geophysical Research Letters* **50**, e2023GL103331. https://doi.org/10.1029/2023GL103331.

Melcher, F., Grum, W., Simon, G., Thalhammer, T. V. & Stumpfl, E. F. (1997). Petrogenesis of the ophiolitic giant chromite deposits of Kempirsai, Kazakhstan: a study of solid and fluid inclusions in chromite. *Journal of Petrology* **38**, 1419–1458. https://doi.org/10.1093/petroj/38.10.1419.

Mendi, D. J., González-Jiménez, J. M., Proenza, J. A., Urbani, F. & Gervilla, F. (2020). Petrogenesis of the chromitite body from the Cerro Colorado ophiolite, Paraguaná Peninsula, Venezuela. *Boletín de la Sociedad Geológica Mexicana* **72**, A280719. https://doi.org/10.18268/BSGM2020v72n3a280719.

Merinero, R., Lunar, R., Ortega, L., Piña, R., Monterrubio, S. & Gervilla, F. (2013). Hydrotermal palladium enrichment in podiform chromitites of Calzadilla de los Barros (SW Iberian Peninsula). *The Canadian Mineralogist* **51**, 387–404. https://doi.org/10.3749/canmin.51.3.387.

Merinero, R., Lunar, R., Ortega, L., Piña, R., Monterrubio, S. & Gervilla, F. (2014). Zoned chromite records multiple metamorphic episodes in the Calzadilla de los Barros ultramafic bodies (SW Iberian peninsula). *European Journal of Mineralogy* **26**, 757–770. https://doi.org/10.1127/ejm/2014/0026-2406.

Merlini, A., Grieco, G. & Diella, V. (2009). Ferritchromite and chromian–chlorite formation in mélange-hosted Kalkan chromitite (Southern Urals, Russia). *American Mineralogist* **94**, 1459–1467. https://doi.org/10.2138/am.2009.3082.

Miller, N. C., Lizarralde, D., Collins, J. A., Holbrook, W. S. & Van Avendonk, H. J. A. (2021). Limited mantle hydration by bending faults at the Middle America Trench. *Journal of Geophysical Research: Solid Earth* **126**, e2020JB020982. https://doi.org/10.1029/2020JB020982.

Muñoz-Montecinos, J., Angiboust, S., Cambeses, A. & Garcia-Casco, A. (2020). Multiple veining in a paleo–accretionary wedge: the metamorphic rock record of prograde dehydration and transient high pore-fluid pressures along the subduction interface (Western Series, Central Chile). *Geosphere* **16**, 765–786. https://doi.org/10.1130/GES02227.1.

Muñoz-Montecinos, J., Angiboust, S., Garcia-Casco, A., Glodny, J. & Bebout, G. (2021). Episodic hydrofracturing and large-scale flushing along deep subduction interfaces: implications for fluid transfer and carbon recycling (Zagros Orogen, southeastern Iran). *Chemical Geology* **571**, 120173. https://doi.org/10.1016/j.chemgeo.2021.120173.

Nishi, M. (2015). Mantle hydration. *Nature Geoscience* **8**, 9–10. https://doi.org/10.1038/ngeo2326.

Novo-Fernández, I., Pujol-Solà, N., Arenas, R., Díez Fernández, R., Proenza, J. A., Rojo-Pérez, E., Cambeses, A., Sánchez Martínez, S., Iglesias, G. & Garcia-Casco, A. (2024). From onset of Cadomian subduction to forearc-arc-continent collision: insights from the Neoproterozoic Calzadilla Metaophiolite (SW Iberia). *International Geology Review* , 1–28.

Penniston-Dorland, S. C., Bebout, G. E., Pogge von Strandmann, P. A. E., Elliott, T. & Sorensen, S. S. (2012a). Lithium and its isotopes as tracers of subduction zone fluids and metasomatic processes: evidence from the Catalina Schist, California, USA. *Geochimica et Cosmochimica Acta* **77**, 530–545. https://doi.org/10.1016/j.gca.2011.10.038.

Penniston-Dorland, S. C., Walker, R. J., Pitcher, L. & Sorensen, S. S. (2012b). Mantle–crust interactions in a paleosubduction zone: evidence from highly siderophile element systematics of eclogite and related rocks. *Earth and Planetary Science Letters* **319-320**, 295–306. https://doi.org/10.1016/j.epsl.2011.11.042.

Penniston-Dorland, S. C., Gorman, J. K., Bebout, G. E., Piccoli, P. M. & Walker, R. J. (2014). Reaction rind formation in the Catalina Schist: deciphering a history of mechanical mixing and metasomatic alteration. *Chemical Geology* **384**, 47–61. https://doi.org/10.1016/j.chemgeo.2014.06.024.

Prigent, C., Warren, J. M., Kohli, A. H. & Teyssier, C. (2020). Fracture-mediated deep seawater flow and mantle hydration on oceanic transform faults. *Earth and Planetary Science Letters* **532**, 115988. https://doi.org/10.1016/j.epsl.2019.115988.

Proenza, J. A., Solé, J. & Melgarejo, J. C. (1999). Uvarovite in podiform chromitite: the Moa-Baracoa massif, Cuba. *The Canadian Mineralogist* **37**, 679–690.

Proenza, J. A., Ortega-Gutiérrez, F., Camprubí, A., Tritlla, J., Elías-Herrera, M. & Reyes-Salas, M. (2004). Paleozoic serpentinite-enclosed chromitites from Tehuitzingo (Acatlán Complex, southern Mexico): a petrological and mineralogical study. *Journal of South American Earth Sciences* **16**, 649–666. https://doi.org/10.1016/j.jsames.2003.12.003.

Proenza, J. A., Zaccarini, F., Escayola, M., Cábana, C., Schalamuk, A. & Garuti, G. (2008). Composition and textures of chromite and platinum-group minerals in chromitites of the western ophiolitic belt from Pampean Ranges of Córdoba, Argentina. *Ore Geology Reviews* **33**, 32–48. https://doi.org/10.1016/j.oregeorev.2006.05.009.

Pujol-Solà, N., Garcia-Casco, A., Proenza, J. A., González-Jiménez, J. M., del Campo, A., Colás, V., Canals, À., Sánchez-Navas, A. & Roqué-Rosell, J. (2020). Diamond forms during low pressure serpentinisation of oceanic lithosphere. *Geochemical Perspectives Letters* **15**, 19–24. https://doi.org/10.7185/geochemlet.2029.

Pujol-Solà, N., Domínguez-Carretero, D., Proenza, J. A., Haissen, F., Ikenne, M., González-Jiménez, J. M., Colás, V., Maacha, L. & Garcia-Casco, A. (2021). The chromitites of the Neoproterozoic Bou Azzer ophiolite (central Anti-Atlas, Morocco) revisited. *Ore Geology Reviews* **134**, 104166. https://doi.org/10.1016/j.oregeorev.2021.104166.

Ramírez-Cárdenas, C. A., Pujol-Solà, N., Proenza, J. A., Weber, M., Castillo-Oliver, M., Tobón, M. & Garcia-Casco, A. (2024). Mantle-hosted ophiolitic chromitites from Colombia: implications for petrogenesis and geodynamic evolution. *International Geology Review* **66**, 81–108. https://doi.org/10.1080/00206814.2023.2228361.

Robinson, P. T., Trumbull, R. B., Schmitt, A., Yang, J.-S., Li, J.-W., Zhou, M.-F., Erzinger, J., Dare, S. & Xiong, F. (2015). The origin and significance of crustal minerals in ophiolitic chromitites and peridotites. *Gondwana Research* **27**, 486–506. https://doi.org/10.1016/j.gr.2014.06.003.

Rollinson, H., Mameri, L. & Barry, T. (2018). Polymineralic inclusions in mantle chromitites from the Oman ophiolite indicate a highly magnesian parental melt. *Lithos* **310-311**, 381–391. https://doi.org/10.1016/j.lithos.2018.04.024.

Shervais, J. W. (2001). Birth, death, and resurrection: the life cycle of suprasubduction zone ophiolites. *Geochemistry, Geophysics, Geosystems* **2**. https://doi.org/10.1029/2000GC000080.

Shervais, J. W., Choi, S. H., Sharp, W. D., Ross, J., Zoglman-Schuman, M. & Mukasa, S. B. (2011) Serpentinite matrix mélange: Implications of mixed provenance for mélange formation. In: Wakabayashi J. & Dilek Y. (eds) *Mélanges: Processes of Formation and Societal Significance*, Geological Society of America Special Papers 480, Geological Society of America, Boulder, CO, pp.1–30.

Sorensen, S. S. & Grossman, J. N. (1989). Enrichment of trace elements in garnet amphibolites from a paleo-subduction zone: Catalina Schist, southern California. *Geochimica et Cosmochimica Acta* **53**, 3155–3177. https://doi.org/10.1016/0016-7037(89)90096-3.

Spear, F. S. (1993) *Metamorphic phase equilibria and pressure-temperature-time paths*. Mineralogical Society of America Monographs, Mineralogical Society of America, Washington, D.C., 799 p.

Spear, F. S., Rumble, D. & Ferry, J. M. (1982) Linear algebraic manipulation of n-dimensional composition space. In: Ferry J. M. (ed) *Characterization of Metamorphism through Mineral Equilibria*, Mineralogical Society of America, Reviews in Mineralogy and Geochemistry, Mineralogical Society of America, Washington, D.C., pp.53–104.

Staudigel, H. & Schreyer, W. (1977). The upper thermal stability of clinochlore, $Mg_5Al[AlSi_3O_{10}](OH)_8$, at 10–35 kb at P_{H2O}. *Contributions to Mineralogy and Petrology* **61**, 187–198. https://doi.org/10.1007/BF00374367.

Suita, M. T. & Strieder, A. J. (1996). Cr-Spinels from Brazilian mafic-ultramafic complexes: metamorphic modifications. *International Geology Review* **38**, 245–267. https://doi.org/10.1080/00206819709465333.

Thompson, J. B. (1982) Composition space: an algebraic and geometric approach. In: Ferry J. M. (ed) *Characterization of metamorphism*

through mineral equilibria. Reviews in Mineralogy and Geochemistry: Mineralogical Society of America, pp.1–31.

Torres-Roldán, R. L. & Garcia-Casco, A. (N.D.) *DWImager: Una implementación para el Procesamiento de Matrices de Intensidades de Rayos X*. Departamento de Mineralogía y Petrología, Universidad de Granada, Granada, Spain.

Torres-Roldan, R. L., Garcia-Casco, A. & Garcia-Sanchez, P. A. (2000). CSpace: an integrated workplace for the graphical and algebraic analysis of phase assemblages on 32-bit wintel platforms. *Computers & Geosciences* **26**, 779–793. https://doi.org/10.1016/S0098-3004(00)00006-6.

Torres-Ruiz, J., Garuti, G., Gazzotti, M., Gervilla, F. & Hach-Ali, P. F. (1996). Platinum-group minerals in chromitites from the ojen lherzolite massif (Serrania de Ronda, Betic Cordillera, Southern Spain). *Mineralogy and Petrology* **56**, 25–50. https://doi.org/10.1007/BF01162656.

Wakabayashi, J. (2011) Mélanges of the Franciscan Complex, California: Diverse structural settings, evidence for sedimentary mixing, and their connection to subduction processes. In: Wakabayashi J. & Dilek Y. (eds) *Mélanges: Processes of Formation and Societal Significance*Geological Society of America Special Papers, Vol. **480**, pp.117–141.

Wakabayashi, J. (2019). Sedimentary compared to tectonically-deformed serpentinites and tectonic serpentinite mélanges at outcrop to petrographic scales: unambiguous and disputed examples from California. *Gondwana Research* **74**, 51–67. https://doi.org/10.1016/j.gr.2019.04.005.

Warr, L. N. (2021). IMA-CNMNC approved mineral symbols. *Mineralogical Magazine* **85**, 291–320. https://doi.org/10.1180/mgm.2021.43.

White, R. W., Powell, R., Holland, T. J. B., Johnson, T. E. & Green, E. C. R. (2014). New mineral activity–composition relations for thermodynamic calculations in metapelitic systems. *Journal of Metamorphic Geology* **32**, 261–286. https://doi.org/10.1111/jmg.12071.

Xiang, H. & Connolly, J. A. D. (2022). GeoPS: an interactive visual computing tool for thermodynamic modelling of phase equilibria. *Journal of Metamorphic Geology* **40**, 243–255. https://doi.org/10.1111/jmg.12626.

Zhang, P.-F., Zhou, M.-F., Liu, Q.-Y., Malpas, J., Robinson, P. T. & He, Y.-S. (2019). Modification of mantle rocks by plastic flow below spreading centers: Fe isotopic and fabric evidence from the Luobusa ophiolite, Tibet. *Geochimica et Cosmochimica Acta* **253**, 84–110. https://doi.org/10.1016/j.gca.2019.03.008.

Zhang, P.-F., Zhou, M.-F., Robinson, P. T., Malpas, J., Yumul, G. P., Wang, C. Y. & Li, J. (2024). Diversities of chromite mineralization induced by chemo–thermal evolution of the mantle during subduction initiation. *Nature Communications* **15**, 9385.

Zhou, M.-F., Robinson, P. T., Su, B.-X., Gao, J.-F., Li, J.-W., Yang, J.-S. & Malpas, J. (2014). Compositions of chromite, associated minerals, and parental magmas of podiform chromite deposits: the role of slab contamination of asthenospheric melts in suprasubduction zone environments. *Gondwana Research* **26**, 262–283. https://doi.org/10.1016/j.gr.2013.12.011.

Zhu, G., Wiens, D. A., Yang, H., Lin, J., Xu, M. & You, Q. (2021). Upper mantle hydration indicated by decreased shear velocity near the Southern Mariana Trench from Rayleigh Wave Tomography. *Geophysical Research Letters* **48**, e2021GL093309. https://doi.org/10.1029/2021GL093309.

Journal of Petrology, 2025, **66**, egaf029
https://doi.org/10.1093/petrology/egaf029
Original Manuscript